Model-Free Predictive Control of DC–DC Boost Converters: Sensor Noise Suppression With Hybrid Extended State Observers

Oluleke Babayomi, *Senior Member, IEEE*, Zhenbin Zhang, *Senior Member, IEEE*, and Zhen Li, *Member, IEEE*

***Abstract*—DC–DC boost converters find versatile application as power conversion interfaces to renewable energy sources including wind, solar photovoltaic, fuel cell, and energy storage systems. The model predictive control (MPC) of these power converters is characterized by multivariable, constrained, optimal control with higher performance than linear control methods. However, MPC is limited by sensor measurement noise and model uncertainties. Although model-free predictive control based on the ultralocal model and conventional extended state observer (MFPC-ESO) can mitigate model uncertainties, MFPC-ESO is limited in noise suppression. Noise suppression is an important control objective in order to keep the steady state ripples bounded and guarantee the stability and robust performance of power converters. Therefore, this study proposes the novel hybrid parallel-cascade ESO, which has better measurement noise suppression than the conventional linear ESO. New higher order hybrid ESO structures are also discussed along with their detailed theoretical analyses. The generalized selection and design guidelines for robust control with measurement noise suppression using hybrid ESOs (including cascade-parallel ESO) are presented. The proposed control schemes are experimentally demonstrated for the robust MFPC of a bidirectional dc–dc boost power converter, under conditions including load, input voltage, measurement noise, and model uncertainties.**

***Index Terms*—DC–DC boost converter, extended state observer (ESO), measurement noise, model predictive control (MPC), model uncertainty, noise suppression, renewable energy sources.**

Manuscript received 16 January 2023; revised 1 April 2023, 14 June 2023, and 4 September 2023; accepted 24 September 2023. Date of publication 2 October 2023; date of current version 6 December 2023. This work was supported in part by the National Key R&D Program of China under Grant 2022YFB4201700, in part by the National Distinguished Expert (YouthTalent) Program of China under Grant 31390089963058, in part by the General Program of National Natural Science Foundation of China under Grants 51977124, 52277191, and 52277192, in part by the Jinan "several Policies on Promoting Collaborative Innovation and Achievement Industrialization of Universities and Research Institutes (Trial)" under Grant 2020GXRC009, in part by the Shenzhen Fundamental Research Program under Grant JCYJ20210324132616040, and in part by the Science Fund for Distinguished Young Scholars of Shandong Province under Grant ZR2023JQ020. Recommended for publication by Associate Editor A. Safaee. *(Corresponding author: Zhenbin Zhang.)*

Oluleke Babayomi is with the Cho Chun Shik Graduate School of Mobility, Korea Advanced Institute of Science and Technology (KAIST), Daejeon 34051, South Korea (e-mail: oluleke.babayomi@mail.sdu.edu.cn).

Zhenbin Zhang and Zhen Li are with the School of Electrical Engineering, Shandong University, Jinan 250061, China (e-mail: zbz@sdu.edu.cn; zhenli0901@sdu.edu.cn).

Color versions of one or more figures in this article are available at https://doi.org/10.1109/TPEL.2023.3321070.

Digital Object Identifier 10.1109/TPEL.2023.3321070

Nomenclature

ADC	Analog-to-digital converter.
BDBC	Bidirectional dc–dc boost power converter.
CESO	Cascade extended state observer.
CP-ESO	Cascade-parallel extended state observer.
ESO	Extended state observer.
ESO-1	Conventional linear extended state observer.
MFPC	Model-free predictive control.
MPC	Model predictive control.
MF-ESO	Multifrequency extended state observer.
PC-ESO	Parallel-cascade extended state observer.

I. Introduction

THE ongoing decarbonization of electrical power generation systems accounts for the growing application of power electronic converters as interfaces to renewable energy sources. These power converters reduce costs and improve the efficiency and reliability of modern energy conversion systems [1]. DC–DC boost converters, in particular, are applied to wind, solar photovoltaic, fuel cell, and energy storage conversion systems. The BDBC facilitates two-way power flow, and steps up the voltage of renewable energy sources. The BDBC operates in the continuous conduction mode or discontinuous conduction mode [2].

MPC of BDBCs is of interest in this study due to its well-reported faster dynamic response than linear control methods. MPC's optimal constrained multiobjective control for pulsed power [3], energy storage [4], fault-tolerant electric vehicle charging [5], and fuel cells [6] has also been reported. Nonetheless, since the prediction model for MPC is strongly dependent on the accuracy of the model (and the measured states), MPC's performance deteriorates with sensor measurement noise and parameter uncertainties. Measurement noise can also lead to instability. Thus, the mitigation of these challenges will decrease the steady state ripples, improve power quality, and guarantee the robustness and stability of MPC for power converters.

The leading types of noise in switch-mode power converters are thermal noise, switching noise, quantization noise, measurement noise, and synchronous sampling errors. Among these, it has been shown that measurement noise can have the most dominant influence on the converter's performance [7]. Measurement noise arises from the practical limitations of signal transducers (including ADCs) and their conditioning circuits.

Although high-resolution ADCs are preferred for improved measurement accuracy, they also increase the system's cost. Hence, lower precision ADCs (16-bits and below) are commonly employed, which can introduce nontrivial measurement noise content to the closed loop. Furthermore, both measurement and quantization noises are random, frequency-independent white noise, which are added to the measured signal [8]. Therefore, attenuating measurement noise also inherently limits quantization noise too, improving the overall noise immunity of the system.

Multirate digital control was proposed for the suppression of switching, quantization, and measurement noises in dual active bridge dc–dc converters [7]. Inoue et al. [9] introduced *LC* low-pass filter function and zero-ripple-current operation to reduce differential- and common-mode switching noises in high-density isolated dc–dc converters. These techniques are not ideal for MPC since they are based on linear control and low-pass filters; the latter slows down the dynamic response.

Bi et al. [10] achieved bidirectional four quadrant MPC for flying capacitor bidirectional buck-boost converter in an energy storage system. The authors in [11] proposed a single-objective cost function (without weighting factor) MPC for multilevel flying-capacitor converter in a microgrid. Nonetheless, the robustness to both parameter uncertainties and measurement noise were neither studied nor tested. Po et al. [12] proposed an adaptive MPC method whereby an observer estimates the real-time values of filter resistance and load resistance. Thus, the controller is updated with the actual values of the parameters to improve robustness to parameter uncertainties. However, the work did not consider load variations and measurement noise, limiting its robustness. A single prediction horizon continuous control-set MPC was proposed by Cheng et al. [13] for the boost converter. Load parameter identification was done with a Luenberger observer to ensure robust control to load uncertainties. However, the work not considers filter parameter mismatches and measurement noise, limiting its robustness. MPC for a boost converter based on continuous and discontinuous conduction models was proposed in [14]. A Kalman observer was applied for improved robustness to load and model uncertainties during current and voltage control [14]. Nonetheless, this solution remains vulnerable to measurement noise. Robust MPC under constant power loads was investigated in [15] for systems that operate in both continuous and discontinuous conduction modes. Voltage regulation and stabilization were ensured even under load changes. However, the study did not investigate the impact of model uncetainties and noise. The MFPC of three-phase interleaved dc–dc boost converters was investigated in [16]. An ultralocal model was utilized to improve the robustness to model uncertainties. However, the influence of measurement noise was not mitigated.

Sawma et al. in [17] proposed a cascaded dual MPC with least mean-square algorithm for online parameter identification. It reported robustness to multiple uncertainties, including sensor noise. Passivity-based MPC relies on power shaping and damping injection to ensure good suppression of noise and parameter mismatch effects [18]. The use of a full-order state observer that filters undesired components from the measured state variable was proposed in [19]. An approximate complex Hall model was employed for MPC control for dc–dc floating interleaved boost converters in [20]. Although the abovementioned schemes improved robustness, their performance is still limited by the strong dependence on model parameters. In summary, the existing body of research literature still lacks solutions to mitigate the combined challenges of model uncertainties and measurement noise in the predictive control of the BDBC.

Measurement noise suppression using the CESO was recently proposed for buck converters [21], [22]. The method was extended to low-power higher order CESO with enhanced rejection of ramp disturbances [23]. The underlying concept supporting CESO was generalized into an MF-ESO model that accommodates other ESO structures including parallel and hybrid ESOs in [24]. The hybrid CP-ESO inherits the noise suppression capabilities of CESO, and gives more superior disturbance rejection than CESO. Furthermore, authors in [24] applied CP-ESO to the MFPC of a grid-connected ac–dc power converter. However, the study did not provide generalized design guidelines for CP-ESO for arbitrary number of subfrequencies. Also, some of the assumptions made for ac–dc converters in [24] cannot hold for dc–dc converters (the focus of this work).

Therefore, the objective of this study is to mitigate both the model uncertainties and measurement noise of the predictive control of BDBCs using hybrid ESOs. The main contributions include the following.

1) A novel hybrid ESO structure is proposed, which has better measurement noise suppression than the ESO-1: the PC-ESO. PC-ESO's theoretical analysis and design procedure are also discussed.
2) Higher order structures for the proposed PC-ESO and CP-ESO are introduced and theoretically analyzed. These lead to generalized selection and design guidelines to achieve effective measurement noise suppression using hybrid PC-ESO and CP-ESO.
3) The hybrid ESOs are experimentally demonstrated for the robust MFPC of a BDBC. To the best of our knowledge, this is the first application of hybrid ESOs to a dc–dc power converter.

The rest of this article is organized as follows. Section II introduces the mathematical problem statement and MF-ESO model. Section III describes the proposed PC-ESO. Section IV discusss higher order hybrid ESO structures and selection guidelines for hybrid ESOs. Section V covers the stability analysis for PC-ESO. Sections VI and VII discuss the MFPC of BDBC with PC-ESO and the experimental validation, respectively. Finally, Section VIII concludes this article.

Notation: In this article, $\mathbb{Z}^+$ is the set of positive nonzero integers. n is the order of the physical system, m is the order of the extended states of the disturbance model, M is the total number of subfrequency levels of the ESO.

II. Preliminaries

In this section, the system to be studied, the relevant challenges, and the state-of-the-art solutions will be briefly discussed.

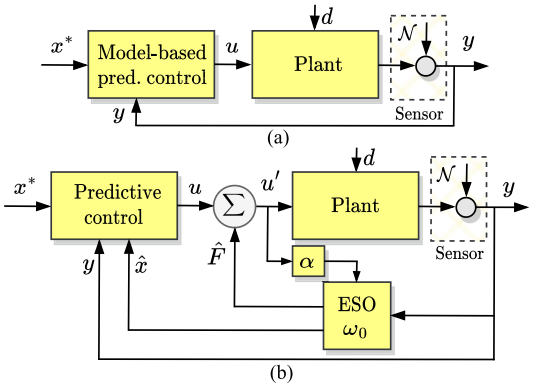

Fig. 1. System description. (a) MPC. (b) Predictive control with ESO-based disturbance estimation.

A. System Description and Problem Statement

Consider a plant whose state x is monitored by a sensor that gives y, which is polluted by sensor noise N [see Fig. 1(a)]. Reference tracking of the system, is achieved by model-based MPC. Two challenges can be associated with this system, viz., 1) sensitivity to parameter variations, and 2) sensor noise pollution. If the model-based state prediction is $x^p(k+1)$, two corresponding types of prediction errors occur: 1) errors from parameter uncertainties $\Delta x_u^p(k+1)$, and 2) errors from measurement noise $\Delta x_h^p(k+1)$, where h represents harmonic frequencies. These cause total prediction error $\Delta x^p(k+1)$

$$\Delta x^p(k+1) = \Delta x_u^p(k+1) + \sum_{h=1}^{\infty} \Delta x_h^p(k+1). \tag{1}$$

Therefore, to improve the prediction accuracy and control performance, it is desirable for $\Delta x^p(k+1) \to 0$. We shall focus on the class of solutions described by (2) (for a single-input single-output first-order system), and illustrated in Fig. 1(b). (2) is an ultralocal model [25]

$$\begin{cases} \dot{x} = F + \alpha u \\ y = x + \mathcal{N} \end{cases} \tag{2}$$

where x is the state, F is the total disturbance, α is a nonzero constant, $\mathcal{N}$ is the measurement noise, u and y are the control input and measured output, respectively.

The closed-loop control input is $u = (\dot{x}^* - \hat{F} - \mathcal{K}(x - x^*))/\alpha$, where $\dot{x}^*$ is the state trajectory, x^* is the state reference, $\hat{F}$ is the estimated total disturbance, and $\mathcal{K}$ is the tracking error gain. The control law requires state estimates via the conventional/standard linear ESO [22]

$$\begin{cases} \dot{\hat{z}} = \hat{F} + \alpha u - \gamma_1(\hat{z} - y) \\ \dot{\hat{F}} = -\gamma_2(\hat{z} - y) \end{cases} \tag{3}$$

where $\{\hat{z}, \hat{F}\}$ are the estimates of $\{x, F\}$, and $\{\gamma_1, \gamma_2\}$ are the observer state error gains. A well-known challenge with the ESO (3) is that it requires high gains for effective disturbance rejection, and this results in high-frequency noise amplification [22]. Attenuating high-frequency noise harmonics is of particular importance for the stability of the linear ESO. Thus, the overall goal of this study is to develop effective control methods to attenuate $\Delta x^p(k+1)$.

B. Multifrequency ESOs

In previous studies, the multifrequency total disturbance model was introduced [24], [26]. Its core features shall be briefly described for the clarity of application to this study.

Given that the ESO is operating at bandwidth ω_0, we can estimate unattenuated components of the total disturbance at subfrequencies less than ω_0. To ease digital computation, we specify these subfrequencies finitely as $\omega_{01} < \omega_{02} < \ldots < \omega_{0\,M} = \omega_0$. Components of F at spectral frequencies $\omega_{0j}\ \forall\ j \in \{1, 2, \ldots, M\}$ can be estimated with a Luenberger type ESO of order m (with state variables $\{f_1, f_2, , \ldots, f_{m-1}\}$). This transforms the system's ultralocal model (2)–(4), and leads to the corresponding ESO (5) for estimating the state and total disturbance components [26]

$$\begin{aligned} \dot{x} &= f_1(\omega_0) + f_1(\omega_{01}, \omega_{02}, \ldots \omega_{0M-1}) + \alpha u \\ \dot{f}_i &= f_{i+1}(\omega_0) + f_{i+1}(\omega_{01}, \omega_{02}, \ldots \omega_{0M-1}) \\ &\qquad (\forall\ i\ \in \{1, 2, \ldots, m-1\}) \\ &\vdots \\ \dot{f}_m &= 0 \\ y &= x + \mathcal{N} \end{aligned} \tag{4}$$

$$\begin{cases} \dot{\hat{x}} = & \sum_{j=1}^{M} \hat{f}_{1,j} + \alpha u - \gamma_m(\hat{x} - y) \\ \dot{\hat{f}}_i = & \sum_{j=1}^{M} \hat{f}_{i+1,j} - \gamma_{m-1}(\hat{x} - y) \\ & \vdots \\ \dot{\hat{f}}_m = & -\gamma_0(\hat{x} - y) \end{cases} \tag{5}$$

where γ_m is the mth observer gain, and all other variables are as previously described. The estimated total disturbance $\hat{F}$ by MF-ESO (5) is then contrived as [26]

$$\hat{F}(t) = \sum_{j=1}^{M} \sum_{i=1}^{m-1} \hat{f}_{i,j}(t). \tag{6}$$

Theoretically, MF-ESO's performance should increase as M increases. However, the increasing complexity may not justify the relative performance improvements. Hence, in practice, $M : M \in \mathbb{Z}^+$ can be constrained to $2 \leq M \leq 4$ for CESO, and $3 \leq M \leq 4$ for hybrid ESOs.

CESO [22], [23] and CP-ESO [24] are two ESOs with noise-attenuating characteristics modeled with (5) that have been proposed in the literature. The structures for CESO and CP-ESO are in Table I. Both CESO and CP-ESO utilize noise-polluted output y at only the lowest subfrequency ω_{01}. Therefore, they avoid noise propagation to higher subfrequency levels of estimation. Their key difference is that for the same $M = 3$ subfrequencies, CESO arranges all three levels in cascade, while CP-ESO has only two cascaded levels.

TABLE I
STRUCTURES OF CESO AND CP-ESO

CESO	CP-ESO
$\begin{cases} \dot{\hat{z}}_1 = \hat{F}_1 + \alpha u - \gamma_{11}(\hat{z}_1 - y) \\ \dot{\hat{F}}_1 = -\gamma_{21}(\hat{z}_1 - y) \\ \dot{\hat{z}}_2 = \hat{F}_2 + \alpha u - \gamma_{12}(\hat{z}_{2.1}) \\ \dot{\hat{F}}_2 = -\gamma_{22}(\hat{z}_{2.1}) \\ \dot{\hat{z}}_3 = \hat{F}_3 + \alpha u - \gamma_{13}(\hat{z}_{3.2}) \\ \dot{\hat{F}}_3 = -\gamma_{23}(\hat{z}_{3.2}) \end{cases}$	$\begin{cases} \dot{\hat{z}}_1 = \hat{F}_1 + \alpha u - \gamma_{11}(\hat{z}_1 - y) \\ \dot{\hat{F}}_1 = -\gamma_{21}(\hat{z}_1 - y) \\ \dot{\hat{z}}_2 = \hat{F}_2 + \alpha u - \gamma_{12}(\hat{z}_{2.1}) \\ \dot{\hat{F}}_2 = -\gamma_{22}(\hat{z}_{2.1}) \\ \dot{\hat{z}}_3 = \hat{F}_3 + \alpha u - \gamma_{13}(\hat{z}_{3.1}) \\ \dot{\hat{F}}_3 = -\gamma_{23}(\hat{z}_{3.1}) \end{cases}$

NB: $\hat{F} = \sum_{j=1}^{3} \hat{F}_j$, $\gamma_{1j} = 2\omega_{0j}$, $\gamma_{2j} = \omega_{0j}^2$ $\forall j \in \{1,2,3\}$, and $\hat{z}_{a.b} = \hat{z}_a - \hat{z}_b$ $\forall\, a, b \in \{1,2,3\}$.

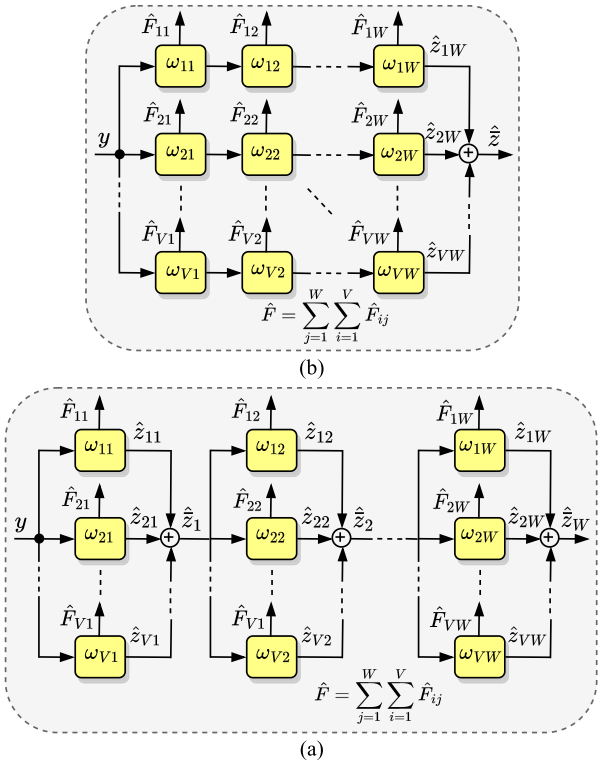

Fig. 2. Structure of the proposed PC-ESO. (a) Conventional CP-ESO. (b) Proposed PC-ESO.

III. PROPOSED PARALLEL-CASCADE ESO

The proposed PC-ESO is formed by arranging strings of cascaded sub-ESOs in parallel branches. A generalized form of PC-ESO is shown in Fig. 2(a), which has V parallel branches, and W cascaded sub-ESOs per branch. Each sub-ESO is tuned to a subfrequency according to the principle of MF-ESO introduced in Section II-B.

PC-ESO is structurally different from CP-ESO [24], which cascades paralleled sub-ESOs [see Fig. 2(b)], producing distinctive time- and frequency-domain characteristics. Fig. 3 shows the structure for $M = 3$ subfrequencies (named PC-ESO-3). PC-ESO-3's time-domain dynamic model is stated in Table II; observer gains are chosen such that the characteristic polynomial $s^2 + \gamma_{1j}s + \gamma_{2j}$ is Hurwitz.

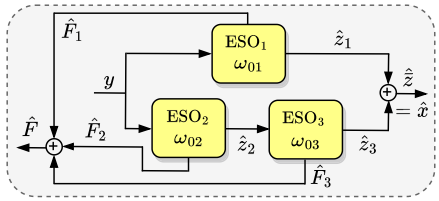

Fig. 3. PC-ESO with three subfrequencies.

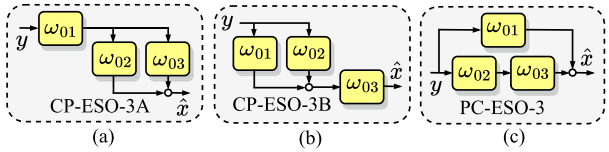

Fig. 4. Hybrid ESO structures with three subfrequency levels. (a)–(b) CP-ESO. (c) PC-ESO.

1) Frequency Domain Transfer Functions: Frequency-domain analysis is facilitated by defining transfer functions from disturbance to estimate errors as $G_{zF}(s) = e_{\hat{z}}(s)/F(s)$, and $G_{FF}(s) = e_{\hat{F}}(s)/F(s)$ (where $e_y = y - \hat{y}$ $\forall\, y \in \{x, F\}$). An effective control law ensures that at steady-state, tracking and estimation errors zero, $y = z^*$. Thus, from the input law in Section II-A, $\alpha u = sy - F$. Noise suppression is analyzed by transfer functions from the measurement noise to estimate errors as $G_{zN}(s) = e_{\hat{z}}(s)/\mathcal{N}(s)$, and $G_{FN}(s) = e_{\hat{F}}(s)/\mathcal{N}(s)$. The full transfer function expressions are stated in Table II, where $\hat{x} = \hat{\bar{z}} = \frac{1}{2}(\hat{z}_1 + \hat{z}_3)$.

A. Comparison With Other Hybrid ESO Structures

Fig. 4 shows possible hybrid ESO structures with $M = 3$ subfrequency levels. Fig. 4(a) and (b) is hybrid CP-ESO structures, while Fig. 4(c) is the proposed PC-ESO. All time-domain expressions are shown in Table II.

For all structures, the observer gains are: $\gamma_{1j} = 2\omega_{0j}$, $\gamma_{2j} = \omega_{0j}^2$, for placement of observer poles at $s = -\omega_{0j}$ $\forall\, j \in \{1,2,3\}$. Each has estimated total disturbance $\hat{F} = \sum_{j=1}^{3} \hat{F}_j$. The states are defined as: $\hat{x} = \frac{1}{2}(\hat{z}_2 + \hat{z}_3)$ (for CP-ESO-3 A), $\hat{x} = \hat{z}_3$ (for CP-ESO-3B), and $\hat{x} = \frac{1}{2}(\hat{z}_1 + \hat{z}_3)$ (for PC-ESO-3).

These three will be further analyzed to distinguish their disturbance estimation and noise suppression characteristics. The full expressions for all transfer functions are in Table II.

1) Frequency Domain Comparison: The Bode plot for $|G_{xF}|$ is shown in Fig. 5(a). At low frequencies, all the hybrid ESOs have lower state error magnitude than CESO-3. PC-ESO-3 and CP-ESO-3B have lower error magnitudes than ESO-1, and the lowest among the three hybrid structures. Thus, the proposed PC-ESO-3 and CP-ESO-3B have the best state estimation performance under disturbance rejection.

The Bode plot of $|G_{FF}|$ [see Fig. 5(a)] indicates that the normalized disturbance estimation error responses for PC-ESO-3 and CP-ESO-3B are consistently lower in magnitude than CESO, ESO-1, and CP-ESO-3B. Furthermore, *the proposed*

TABLE II
TIME- AND FREQUENCY-DOMAIN EXPRESSIONS FOR HYBRID ESOS ($M = 3$)

	PC-ESO-3	**CP-ESO-3A**	**CP-ESO-3B**
ESO Structure	$\begin{cases}\dot{\hat{z}}_1 = \hat{F}_1 + \alpha u - \gamma_{11}(\hat{z}_1 - y)\\ \dot{\hat{F}}_1 = -\gamma_{21}(\hat{z}_1 - y)\\ \dot{\hat{z}}_2 = \hat{F}_2 + \alpha u - \gamma_{12}(\hat{z}_2 - y)\\ \dot{\hat{F}}_2 = -\gamma_{22}(\hat{z}_2 - y)\\ \dot{\hat{z}}_3 = \hat{F}_3 + \alpha u - \gamma_{13}(\hat{z}_3 - \hat{z}_2)\\ \dot{\hat{F}}_3 = -\gamma_{23}(\hat{z}_3 - \hat{z}_2)\end{cases}$	$\begin{cases}\dot{\hat{z}}_1 = \hat{F}_1 + \alpha u - \gamma_{11}(\hat{z}_1 - y)\\ \dot{\hat{F}}_1 = -\gamma_{21}(\hat{z}_1 - y)\\ \dot{\hat{z}}_2 = \hat{F}_2 + \alpha u - \gamma_{12}(\hat{z}_2 - \hat{z}_1)\\ \dot{\hat{F}}_2 = -\gamma_{22}(\hat{z}_2 - \hat{z}_1)\\ \dot{\hat{z}}_3 = \hat{F}_3 + \alpha u - \gamma_{13}(\hat{z}_3 - \hat{z}_1)\\ \dot{\hat{F}}_3 = -\gamma_{23}(\hat{z}_3 - \hat{z}_1)\end{cases}$	$\begin{cases}\dot{\hat{z}}_1 = \hat{F}_1 + \alpha u - \gamma_{11}(\hat{z}_1 - y)\\ \dot{\hat{F}}_1 = -\gamma_{21}(\hat{z}_1 - y)\\ \dot{\hat{z}}_2 = \hat{F}_2 + \alpha u - \gamma_{12}(\hat{z}_2 - y)\\ \dot{\hat{F}}_2 = -\gamma_{22}(\hat{z}_2 - y)\\ \dot{\hat{z}}_3 = \hat{F}_3 + \alpha u - \gamma_{13}(\hat{z}_3 - \hat{z}_{s12})\\ \dot{\hat{F}}_3 = -\gamma_{23}(\hat{z}_3 - \hat{z}_{s12})\end{cases}$
G_{xF}	$-\frac{1}{2}s[\zeta_1^{-1} + (s^2 + 2(\omega_{02} + \omega_{03})s + \omega_{02}^2 + \omega_{03}^2)\zeta_2^{-1}\zeta_3^{-1}]$	$-\frac{1}{2}s[(s^2 + 2(\omega_{01} + \omega_{02})s + \omega_{01}^2 + \omega_{02}^2)\zeta_1^{-1}\zeta_2^{-1} + (s^2 + 2(\omega_{01} + \omega_{03})s + \omega_{01}^2 + \omega_{03}^2)\zeta_1^{-1}\zeta_3^{-1}]$	$-\frac{1}{2}s[(s^2 + 2(\omega_{01} + \omega_{03})s + \omega_{01}^2 + \omega_{03}^2)\zeta_1^{-1}\zeta_3^{-1} + (s^2 + 2(\omega_{02} + \omega_{03})s + \omega_{02}^2 + \omega_{03}^2)\zeta_2^{-1}\zeta_3^{-1}]$
G_{FF}	$1 - \frac{1}{3}[\omega_{01}^2\zeta_1^{-1} + \omega_{02}^2\zeta_2^{-1} + \omega_{03}^2(2\omega_{02}s + \omega_{02}^2)\zeta_2^{-1}\zeta_3^{-1}]$	$1 - \frac{1}{3}[\omega_{01}^2\zeta_1^{-1} + \omega_{02}^2(2\omega_{01}s + \omega_{01}^2)\zeta_1^{-1}\zeta_2^{-1} + \omega_{02}^2(2\omega_{02}s + \omega_{02}^2)\omega_{01}^{-1}\omega_{03}^{-1}]$	$1 - \frac{1}{4}[\omega_{01}^2\zeta_1^{-1} + \omega_{02}^2\zeta_2^{-1} + \omega_{03}^2(2\omega_{01}s + \omega_{01}^2)\zeta_1^{-1}\zeta_3^{-1} + \omega_{03}^2(2\omega_{02}s + \omega_{02}^2)\omega_{02}^{-1}\omega_{03}^{-1}]$
G_{xN}	$-\frac{1}{2}[(2\omega_{01}s + \omega_{01}^2)(2\omega_{03}s + \omega_{03}^2)\zeta_1^{-1}\zeta_3^{-1} + (2\omega_{02}s + \omega_{02}^2)\zeta_2^{-1}]$	$-\frac{1}{2}[(2\omega_{01}s + \omega_{01}^2)(2\omega_{02}s + \omega_{02}^2)\zeta_1^{-1}\zeta_2^{-1} + (2\omega_{01}s + \omega_{01}^2)(2\omega_{03}s + \omega_{03}^2)\zeta_1^{-1}\zeta_3^{-1}]$	$-\frac{1}{2}[(2\omega_{01}s + \omega_{01}^2)(2\omega_{03}s + \omega_{03}^2)\zeta_1^{-1}\zeta_3^{-1} + (2\omega_{02}s + \omega_{02}^2)(2\omega_{03}s + \omega_{03}^2)\zeta_2^{-1}\zeta_3^{-1}]$
G_{FN}	$-s[\omega_{01}^2\zeta_1^{-1} + (2\omega_{01}s + \omega_{01}^2)\omega_{03}^2\zeta_1^{-1}\zeta_3^{-1} + \omega_{02}^2\zeta_2^{-1}]$	$-s[\omega_{01}^2\zeta_1^{-1} + \omega_{02}^2(2\omega_{01}s + \omega_{01}^2)\zeta_1^{-1}\zeta_2^{-1} + \omega_{03}^2(2\omega_{01}s + \omega_{01}^2)\zeta_1^{-1}\zeta_3^{-1}]$	$-s[\omega_{01}^2\zeta_1^{-1} + \omega_{02}^2\zeta_2^{-1} + \frac{1}{2}(2\omega_{01}s + \omega_{01}^2)\omega_{03}^2\zeta_1^{-1}\zeta_3^{-1} + (2\omega_{02}s + \omega_{02}^2)\omega_{03}^2\zeta_2^{-1}\zeta_3^{-1}]$

NB: $\hat{F} = \sum_{j=1}^{3}\hat{F}_j$, $\gamma_{1j} = 2\omega_{0j}$, $\gamma_{2j} = \omega_{0j}^2\ \forall\, j \in \{1, 2, 3\}$. $\hat{z}_{s12} = \hat{z}_1 + \hat{z}_2$, $\zeta_1 = (s + \omega_{01})^2$, $\zeta_2 = (s + \omega_{02})^2$, and $\zeta_3 = (s + \omega_{03})^2$.

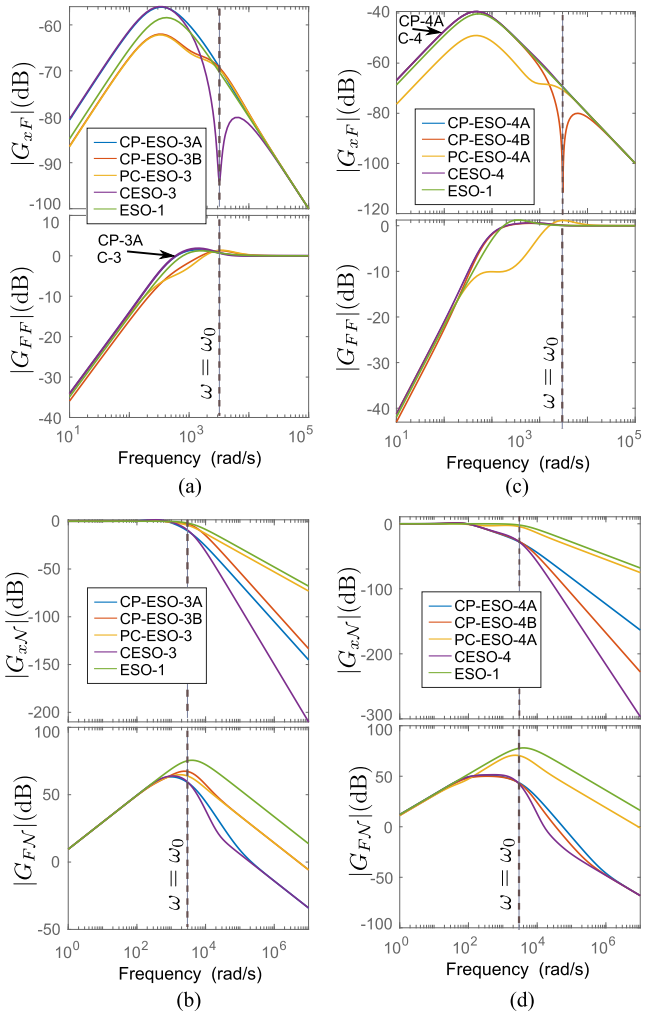

Fig. 5. Bode magnitude plots of $G_{xF}(s)$, $G_{FF}(s)$, $G_{xN}(s)$, and $G_{FN}(s)$. (a), (b) $M = 3$. (c), (d) $M = 4$.

PC-ESO-3 has the lowest tracking error among the three hybrid ESOs.

The noise suppression frequency characteristics are shown by Bode magnitude plots of $G_{x\mathcal{N}}$, and $G_{F\mathcal{N}}$. Although the CP-ESOs have the best noise suppression performance in both plots, the proposed PC-ESO has consistently better noise suppression than conventional ESO-1. For $G_{x\mathcal{N}}$, CP-ESO-3B has a similar slope of -40 dB/decade as CP-ESO-3 A (the latter has a lower gain at all mid- to high-frequencies). PC-ESO-3's slope of -20 dB/decade, is identical to ESO-1's, but with lower estimation error than ESO-1 at mid- to high-frequencies. Similarly, the Bode plot for $G_{F\mathcal{N}}$ shows that total disturbance estimation error follows the same trend as state estimation: all three hybrid ESOs have better noise suppression than ESO-1.

B. PC-ESO Parameter Design Guidelines

1) Gain Parameter Tuning: Bandwidth parameterization [27] simplifies the tuning of PC-ESO's gain parameters $\{\gamma_{1j}, \gamma_{2j}\}$ for poles placement at $s = -\omega_{0j}$. The gains are: $\gamma_{1j} = 2\omega_{0j}$, $\gamma_{2j} = \omega_{0j}^2\ \forall\, j \in \{1, 2, 3\}$. The subfrequencies ω_{0j} are determined by the following subfrequency guidelines.

2) Design Guidelines for Subfrequencies:

a) ω_0: The bandwidth ω_0 is chosen according the desired system response; higher bandwidths give faster dynamic responses. Nonetheless, as ω_0 increases, high-frequency noise amplification worsens [22].

b) ω_{01}: Among all the subfrequencies ω_{01} has the strongest influence on the magnitude of noise suppression; noise suppression improves as ω_{01} decreases [see Fig. 6(a)]. However, to prevent interphase distortions, a minimum value of $\omega_{01} = \frac{\omega_0}{M^3}$ is recommended.

c) Intermediate subfrequencies between ω_{01} and ω_0: The plot of $|G_{xN}|$ in Fig. 6(b) indicates that under noisy conditions high-frequency state estimation error decreases as ω_{02}

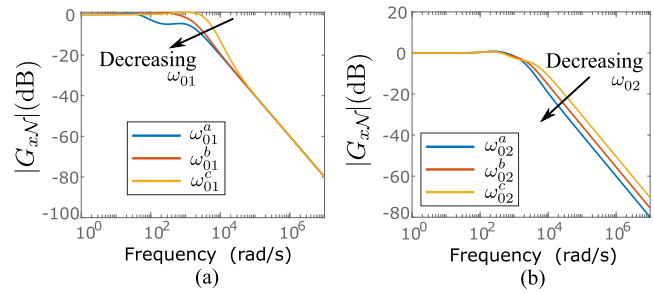

Fig. 6. Bode plots for the variation of subfrequencies. (a) ω_{01} is varied. $[\omega_{01}^a, \omega_{01}^b, \omega_{01}^c] = [\frac{\omega_0}{M^4}, \frac{\omega_0}{M^2}, \frac{\omega_0}{1.05}]$. (b) ω_{02} is varied: $[\omega_{02}^a, \omega_{02}^b, \omega_{02}^c] = [\frac{\omega_0}{M}, \frac{\omega_0(1+M^2)}{2\,M^2}, 0.9\omega_0]$; ω_{02}^b lies at the midpoint between ω_{01} and ω_{03}.

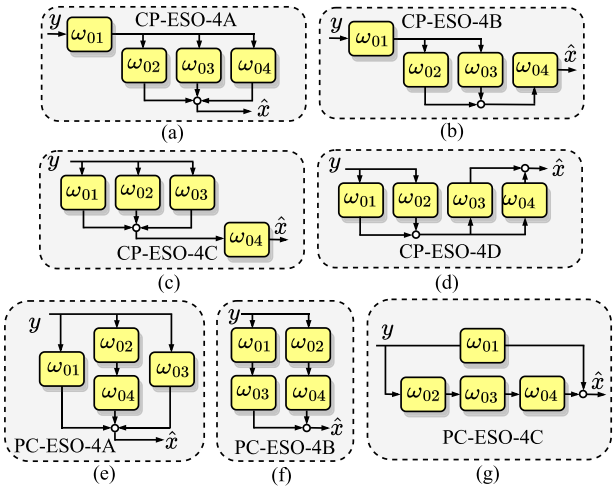

Fig. 7. Proposed hybrid ESO structures with four subfrequency levels. (a)–(d) Hybrid CP-ESO structures. (e)–(g) hybrid PC-ESO structures.

decreases. Therefore, lower values of ω_{02} are preferred—in contrast to CP-ESO that is better with ω_{02} being equidistant in the interval between ω_{01} and ω_0 [26].

Based on the abovementioned guidelines, the subfrequencies for experimental verification in this study are

$$[\omega_{01}, \omega_{02}, \omega_{03}] = \left[\frac{\omega_0}{M^2},\ \frac{\omega_0}{M},\ \omega_0\right] \tag{7}$$

where $M = 3$ for noise suppression (except otherwise stated), and $M = 1.05$ when noise suppression is not required.

IV. Proposed Higher-Order Hybrid ESO Structures

The analysis in Section III-B points to the potential of hybrid ESOs for robust control with noise suppression, namely: i) better noise suppression than the conventional ESO, and ii) better disturbance rejection than CESO. Therefore, design guidelines for selecting the best hybrid ESO for different applications are necessary. In order to deduce generalized design guidelines, we will briefly investigate the characteristics of higher order hybrid ESO structures.

Fig. 7 shows seven possible hybrid ESO structures with $M = 4$ subfrequency levels. Fig. 7(a)–(d) are hybrid CP-ESO structures, while Fig. 7(e)–(g) are hybrid PC-ESO structures. The subfrequencies are arranged such that the noisy measured output y is first fed into the lowest frequencies to enhance noise suppression. Time-domain equations for the hybrid ESOs are shown in Table III.

For all structures, the observer gains are: $\gamma_{1j} = 2\omega_{0j}$, $\gamma_{2j} = \omega_{0j}^2$, for placement of observer poles at $s = -\omega_{0j}\ \forall\ j \in \{1, 2, 3, 4\}$. Each has estimated total disturbance of $\hat{F} = \sum_{j=1}^{4} \hat{F}_j$. In order to highlight unique characteristics that will lead to generalizable conclusions, we shall focus on three out of seven structures: CP-ESO-4 A [see Fig. 7(a)], CP-ESO-4B [see Fig. 7(b)], and PC-ESO-4 A [see Fig. 7(e)]. The states are defined as: $\hat{x} = \frac{1}{3}(\hat{z}_2 + \hat{z}_3 + \hat{z}_4)$ (for CP-ESO-4 A), $\hat{x} = \hat{z}_4$ (for CP-ESO-4B), and $\hat{x} = \frac{1}{3}(\hat{z}_1 + \hat{z}_3 + \hat{z}_4)$ (for PC-ESO-4 A). Further analyses of the structures will distinguish their disturbance estimation and noise suppression characteristics.

1) Frequency Domain Transfer Functions: The frequency-domain transfer functions from disturbance to estimate errors are: $G_{xF}(s) = e_{\hat{x}}(s)/F(s)$, and $G_{FF}(s) = e_{\hat{F}}(s)/F(s)$ (where $e_y = y - \hat{y}\ \forall\ y \in \{x, F\}$). Noise suppression is analyzed by transfer functions from the measurement noise to estimate errors as $G_{xN}(s) = e_{\hat{x}}(s)/\mathcal{N}(s)$, and $G_{FN}(s) = e_{\hat{F}}(s)/\mathcal{N}(s)$. Full expressions for the transfer functions are shown in Table III.

2) Frequency Domain Comparison: The Bode plots for transfer functions, for the case of four subfrequency levels are shown in Fig. 5(c), (d). In the plots of $|G_{xF}|$, at low frequencies, PC-ESO-4 A has the lowest state estimation error magnitude among the hybrid structures. All plots converge in the high-frequency region. At $\omega = \omega_0$, CP-ESO-4B manifests a notch characteristic which makes the noise error magnitude to become significantly attenuated. The Bode plot of $|G_{FF}|$ also indicates that the disturbance estimation error response for PC-ESO-4 is consistently lower in magnitude than other hybrid structures between $\omega_{01} < \omega < \omega_{03}$. In summary, PC-ESO-4 A has the most consistently superior disturbance rejection among the hybrid structures in all frequency regions.

The noise suppression capability is shown by Bode magnitude plots of $G_{x\mathcal{N}}$, and $G_{F\mathcal{N}}$. $|G_{x\mathcal{N}}|$ shows that in the mid- to high-frequency regions, CP-ESO-4B, has the steepest run-off slope of -60 dB/decade. CP-ESO-4 A also has a modest slope of -40 dB/decade, while PC-ESO-4 A has the least desirable slope of -20 dB/decade. Hence, PC-ESO-4 A has poorer noise suppression than the other two hybrid structures. In summary, CP-ESO-4B has the best noise suppression performance. Similarly, the Bode plot for $G_{F\mathcal{N}}$ shows that total disturbance estimation error follows the same trend as for state-performance: all three hybrid ESOs have better noise suppression than ESO-1, and CP-ESO-4B has the lowest error magnitude of all three hybrid ESOs.

Remark: The hybrid schemes generally have better high-frequency noise suppression than ESO-1. They also have better low-frequency total disturbance estimation than CESO. Therefore, they give *hybrid-frequency characteristics that neither ESO-1 or CESO can produce alone.*

B. Generalized Hybrid ESO Selection/Design Guidelines

The foregoing analyses, lead to the following three structural design principles for hybrid ESOs, viz.,

TABLE III
TRANSFER FUNCTIONS FOR HYBRID ESOS WITH FOUR SUB-FREQUENCY LEVELS $M = 4$

	CP-ESO-4A	**CP-ESO-4B**	**PC-ESO-4A**
ESO Structure	$\begin{cases}\dot{\hat{z}}_1 = \hat{F}_1 + \alpha u - \gamma_{11}(\hat{z}_1 - y)\\ \dot{\hat{F}}_1 = -\gamma_{21}(\hat{z}_1 - y)\\ \dot{\hat{z}}_2 = \hat{F}_2 + \alpha u - \gamma_{12}(\hat{z}_2 - \hat{z}_1)\\ \dot{\hat{F}}_2 = -\gamma_{22}(\hat{z}_2 - \hat{z}_1)\\ \dot{\hat{z}}_3 = \hat{F}_3 + \alpha u - \gamma_{13}(\hat{z}_3 - \hat{z}_1)\\ \dot{\hat{F}}_3 = -\gamma_{23}(\hat{z}_3 - \hat{z}_1)\\ \dot{\hat{z}}_4 = \hat{F}_4 + \alpha u - \gamma_{14}(\hat{z}_4 - \hat{z}_1)\\ \dot{\hat{F}}_4 = -\gamma_{24}(\hat{z}_4 - \hat{z}_1)\end{cases}$	$\begin{cases}\dot{\hat{z}}_1 = \hat{F}_1 + \alpha u - \gamma_{11}(\hat{z}_1 - y)\\ \dot{\hat{F}}_1 = -\gamma_{21}(\hat{z}_1 - y)\\ \dot{\hat{z}}_2 = \hat{F}_2 + \alpha u - \gamma_{12}(\hat{z}_2 - \hat{z}_1)\\ \dot{\hat{F}}_2 = -\gamma_{22}(\hat{z}_2 - \hat{z}_1)\\ \dot{\hat{z}}_3 = \hat{F}_3 + \alpha u - \gamma_{13}(\hat{z}_3 - \hat{z}_1)\\ \dot{\hat{F}}_3 = -\gamma_{23}(\hat{z}_3 - \hat{z}_1)\\ \dot{\hat{z}}_4 = \hat{F}_4 + \alpha u - \gamma_{14}(\hat{z}_4 - \hat{z}_{s23})\\ \dot{\hat{F}}_4 = -\gamma_{24}(\hat{z}_4 - \hat{z}_{s23})\end{cases}$	$\begin{cases}\dot{\hat{z}}_1 = \hat{F}_1 + \alpha u - \gamma_{11}(\hat{z}_1 - y)\\ \dot{\hat{F}}_1 = -\gamma_{21}(\hat{z}_1 - y)\\ \dot{\hat{z}}_2 = \hat{F}_2 + \alpha u - \gamma_{12}(\hat{z}_2 - y)\\ \dot{\hat{F}}_2 = -\gamma_{22}(\hat{z}_2 - y)\\ \dot{\hat{z}}_3 = \hat{F}_3 + \alpha u - \gamma_{13}(\hat{z}_3 - y)\\ \dot{\hat{F}}_3 = -\gamma_{23}(\hat{z}_3 - y)\\ \dot{\hat{z}}_4 = \hat{F}_4 + \alpha u - \gamma_{14}(\hat{z}_4 - \hat{z}_2)\\ \dot{\hat{F}}_4 = -\gamma_{24}(\hat{z}_4 - \hat{z}_2)\end{cases}$
G_{xF}	$-s[(s^2 + 2(\omega_{01} + \omega_{02})s + \omega_{01}^2 + \omega_{02}^2)\zeta_1^{-1}\zeta_2^{-1} + (s^2 + 2(\omega_{01} + \omega_{03})s + \omega_{01}^2 + \omega_{03}^2)\zeta_1^{-1}\zeta_3^{-1} + (s^2 + 2(\omega_{01} + \omega_{04})s + \omega_{01}^2 + \omega_{04}^2)\zeta_1^{-1}\zeta_4^{-1}]$	$-s[(2\omega_{04} + \omega_{04}^2)(s^2 + 2(\omega_{01} + \omega_{02})s + \omega_{01}^2 + \omega_{02}^2 + \zeta_1\zeta_2)\zeta_1^{-1}\zeta_2^{-1}\zeta_4^{-1} + (2\omega_{04} + \omega_{04}^2)(s^2 + 2(\omega_{01} + \omega_{03})s + \omega_{01}^2 + \omega_{03}^2 + \zeta_1\zeta_3)\zeta_1^{-1}\zeta_3^{-1}\zeta_4^{-1}]$	$-s[\zeta_1^{-1} + (s^2 + 2(\omega_{02} + \omega_{04})s + \omega_{02}^2 + \omega_{04}^2)\zeta_2^{-1}\zeta_4^{-1} + \zeta_3^{-1}]$
G_{FF}	$1 - \frac{1}{4}[\omega_{01}^2\zeta_1^{-1} + \omega_{02}^2(2\omega_{01}s + \omega_{01}^2)\zeta_1^{-1}\zeta_2^{-1} + \omega_{03}^2(2\omega_{01}s + \omega_{01}^2)\zeta_1^{-1}\zeta_3^{-1} + \omega_{04}^2(2\omega_{01}s + \omega_{01}^2)\zeta_1^{-1}\zeta_4^{-1}]$	$1 - \frac{1}{5}[\omega_{01}^2\zeta_1^{-1} + \omega_{02}^2(2\omega_{01}s + \omega_{01}^2)\zeta_1^{-1}\zeta_2^{-1} + \omega_{03}^2(2\omega_{01}s + \omega_{01}^2)\zeta_1^{-1}\zeta_3^{-1} + (-\omega_{04}^2 s^2(s^2 + 2(\omega_{01} + \omega_{02})s + \omega_{01}^2 + \omega_{02}^2) + \omega_{04}^2\zeta_1\zeta_2)\zeta_1^{-1}\zeta_2^{-1}\zeta_4^{-1} + (-\omega_{04}^2 s^2(s^2 + 2(\omega_{01} + \omega_{03})s + \omega_{01}^2 + \omega_{03}^2) + \omega_{04}^2\zeta_1\zeta_3)\zeta_1^{-1}\zeta_3^{-1}\zeta_4^{-1}]$	$1 - \frac{1}{4}[\omega_{01}^2\zeta_1^{-1} + \omega_{02}^2\zeta_2^{-1} + \omega_{03}^2\zeta_3^{-1} + \omega_{04}^2(2\omega_{02}s + \omega_{02}^2)\zeta_2^{-1}\zeta_4^{-1}]$
G_{xN}	$-(2\omega_{01}s + \omega_{01}^2)[(2\omega_{02}s + \omega_{02}^2)\zeta_1^{-1}\zeta_2^{-1} + (2\omega_{03}s + \omega_{03}^2)\zeta_1^{-1}\zeta_3^{-1} + (2\omega_{04}s + \omega_{04}^2)\zeta_1^{-1}\zeta_4^{-1}]$	$-(2\omega_{01}s + \omega_{01}^2)(2\omega_{04}s + \omega_{04}^2)[(2\omega_{02}s + \omega_{02}^2)\zeta_1^{-1}\zeta_2^{-1}\zeta_4^{-1} + (\omega_{03}s + \omega_{03}^2)\zeta_1^{-1}\zeta_3^{-1}\zeta_4^{-1}]$	$-[(\omega_{01}s + \omega_{01}^2)\zeta_1^{-1} + (2\omega_{02}s + \omega_{02}^2)(2\omega_{04}s + \omega_{04}^2)\zeta_2^{-1}\zeta_4^{-1} + (2\omega_{03}s + \omega_{03}^2)\zeta_3^{-1}]$
G_{FN}	$-s[\omega_{01}^2\zeta_1^{-1} + \omega_{02}^2(2\omega_{01}s + \omega_{01}^2)\zeta_1^{-1}\zeta_2^{-1} + \omega_{03}^2(2\omega_{01}s + \omega_{01}^2)\zeta_1^{-1}\zeta_3^{-1} + \omega_{04}^2(2\omega_{01}s + \omega_{01}^2)\zeta_1^{-1}\zeta_4^{-1}]$	$-s[\omega_{01}^2\zeta_1^{-1} + \omega_{02}^2(2\omega_{01}s + \omega_{01}^2)\zeta_1^{-1}\zeta_2^{-1} + \omega_{03}^2(2\omega_{01}s + \omega_{01}^2)\zeta_1^{-1}\zeta_3^{-1} + \frac{1}{2}\omega_{04}^2(2\omega_{01}s + \omega_{01}^2)((2\omega_{02}s + \omega_{02}^2)\zeta_1^{-1}\zeta_2^{-1}\zeta_4^{-1} + (2\omega_{03}s + \omega_{03}^2)\zeta_1^{-1}\zeta_3^{-1}\zeta_4^{-1})]$	$-s[\omega_{01}^2\zeta_1^{-1} + \omega_{04}^2(2\omega_{02}s + \omega_{02}^2)\zeta_2^{-1}\zeta_4^{-1} + \omega_{03}^2\zeta_3^{-1}]$

NB: $\hat{F} = \sum_{j=1}^{4}\hat{F}_j$, $\hat{z}_{s23} = \hat{z}_2 + \hat{z}_3$, $\zeta_1 = (s + \omega_{01})^2$, $\zeta_2 = (s + \omega_{02})^2$, $\zeta_3 = (s + \omega_{03})^2$, and $\zeta_4 = (s + \omega_{04})^2$.

1) The noise suppression improves as we: i) decrease the number of subfrequency levels that receive the measured noisy signal y, and ii) pass y through the lowest subfrequencies in the ESO.
2) Higher numbers of cascaded levels (as in CP-ESOs) increase the noise suppression, but reduce disturbance rejection performance.
3) Higher numbers of paralleled levels (as in PC-ESOs) increase the disturbance rejection.

V. STABILITY ANALYSIS

Let $e_\sigma = \sigma - \hat{\sigma}$ ($\sigma = \{z, F\}$) be the estimation error. Without loss of generality, the analysis is for a case when the proposed PC-ESO has V parallel branches and two cascaded sub-ESOs per branch. The estimation error dynamics is

$$\dot{\mathbf{e}}_\sigma = \mathbf{A}_e\mathbf{e}_\sigma + \mathbf{E}\nu(\omega_{\text{res}}) - \mathbf{L}\mathcal{N} \tag{8}$$

where $\nu(\omega_{\text{res}})$ is the residual unestimated total disturbance at residual frequencies ω_{res}, $\mathcal{N}$ is the measurement noise, $\mathbf{E} = [\mathbf{0}_{1\times(4V-1)}, 1]^\top$, $e_\sigma = \sigma - \hat{\sigma}$ ($\sigma = [\hat{z}_{11}, \hat{F}_{11}, \hat{z}_{12}, \hat{F}_{12}, \hat{z}_{21}, \hat{F}_{21}, \hat{z}_{22}, \hat{F}_{22}, \ldots, \hat{z}_{V1}, \hat{F}_{V1}, \hat{z}_{V2}, \hat{F}_{V2}]^\top$), $\mathbf{L} = [l_{11}\omega_0, l_{11}\omega_0^2, l_{12}\omega_0, l_{12}\omega_0^2, l_{21}\omega_0, l_{21}\omega_0^2, l_{22}\omega_0, l_{22}\omega_0^2, \ldots, l_{V1}\omega_0, l_{V1}\omega_0^2, l_{V2}\omega_0, l_{V2}\omega_0^2,]^\top$

$$\mathbf{A}_e = \begin{bmatrix} \mathbf{a}_{e.11} & 0 & 0 & 0 & \ldots & 0 & 0 \\ 0 & \mathbf{a}_{e.12} & 0 & 0 & \ldots & 0 & 0 \\ 0 & 0 & \mathbf{a}_{e.21} & 0 & \ldots & 0 & 0 \\ 0 & 0 & 0 & \mathbf{a}_{e.22} & \ldots & 0 & 0 \\ \vdots & \vdots & \vdots & \vdots & \ddots & 0 & 0 \\ 0 & 0 & 0 & 0 & \ldots & \mathbf{a}_{e.V1} & 0 \\ 0 & 0 & 0 & 0 & \ldots & 0 & \mathbf{a}_{e.V2} \end{bmatrix} \tag{9}$$

and $\mathbf{a}_{e.ij} = \begin{bmatrix} -l_{i1}\omega_0 & 1 \\ -l_{i2}\omega_0^2 & 0 \end{bmatrix}$, $\forall\, i \in \{1, 2, \ldots, V\}$, and $j \in \{1, 2\}$. The observer parameters l_{ij} are selected such that $\mathbf{A}_e$ is Hurwitz.

Proposition: The system defined by (8) which has state $\mathbf{e}_\sigma$ and input $\mathcal{N}$ is input-to-state (ISS) stable.

Proof: We shall apply a change of variable to the scaled error vector

$$\mathbf{e}_\sigma \to \mathbf{\Psi} := \mathcal{K}\mathbf{e}_\sigma \tag{10}$$

where $\mathcal{K} := \text{blkdiag}(\mathcal{K}_0, \mathcal{K}_1, \ldots, \mathcal{K}_M)$, and $\mathcal{K}_j := \text{diag}(\omega_0^{-(j-1)}, \omega_0^{-j}, \omega_0^{-(j-1)}, \omega_0^{-j})$. So, (8) becomes

$$\begin{aligned}\dot{\mathbf{\Psi}} &= \mathcal{K}\mathbf{A}_e\mathcal{K}^{-1}\mathbf{\Psi} + \mathcal{K}\mathbf{E}\nu - \mathcal{K}\mathbf{L}\mathcal{N} \\ &= \omega_0\mathbf{H}\mathbf{\Psi} + \omega_0^{-M}\mathbf{E}\nu - \omega_0\bar{\mathbf{L}}\mathcal{N}\end{aligned} \tag{11}$$

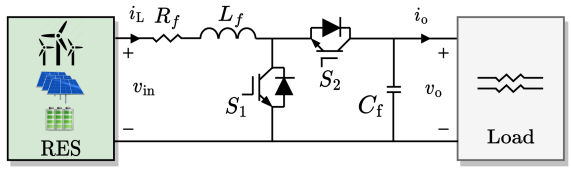

Fig. 8. Bidirectional DC–DC boost converter.

where $\mathbf{H} = \mathbf{A}_e$ for $\omega_0 = 1$ in (9).

Assumption 1: The mth-order derivative of F ($F^{(m)} = \nu(\omega_{\text{res}})$) is bounded such that $|\nu| \leq \epsilon_1$.

Assumption 2: Output sensor measurement noise $\mathcal{N}$ is bounded such that $|\mathcal{N}| \leq \epsilon_2$.

Let $W = \mathbf{\Psi}^\top \mathbf{R} \mathbf{\Psi}$ be a Lyapunov function within range $\lambda_1 \|\mathbf{\Psi}\|^2 \leq W \leq \lambda_2 \|\mathbf{\Psi}\|^2$, where λ_1, λ_2 are, respectively, the smallest and largest eigenvalues of a symmetric positive-definite matrix $\mathbf{R}$, which is a solution to $\mathbf{RH} + \mathbf{H}^\top \mathbf{R} = -\mathbf{I}$. The derivative of W based on (11) gives

$$\dot{W} \leq -\omega_0 \|\mathbf{\Psi}\|^2 + 2\omega_0^{-M} |\nu| \|\mathbf{R}\| \|\mathbf{\Psi}\| + 2\omega_0 |\mathcal{N}| \|\mathbf{R}\bar{\mathbf{L}}\| \|\mathbf{\Psi}\| \tag{12}$$

so that

$$\begin{aligned} \dot{W} \leq & -(1-\chi)|\omega_0| \|\mathbf{\Psi}\|^2 \\ & \forall \|\mathbf{\Psi}\| \geq \chi_{\epsilon 1} \omega_0^{-(M+1)} + \chi_{\epsilon 2} \|\mathbf{R}\bar{\mathbf{L}}\| \end{aligned} \tag{13}$$

where $\chi \in (0,1)$ is a constant, $\chi_{\epsilon 1} = \frac{2\lambda_1 \epsilon_1}{\chi}$, and $\chi_{\epsilon 2} = \frac{2\epsilon_2}{\chi}$. Based on *Assumptions 1, 2*, the lower bound of $\|\mathbf{\Psi}\|$ belongs to a class of strictly increasing functions with zero-value at the origin [21]. Invoking the comprehensive definition of ISS stability in [21], the system (8) is ISS stable. ■

VI. Power Converter Modeling and Control

In this section, the models for model-based and proposed MFPC with noise suppression will be formulated.

A. Model-Based Predictive Control

The bidirectional boost converter (see Fig. 8) has the following continuous conduction mode model:

$$\begin{cases} L_f \frac{di_L}{dt} = & v_{in} - R_f i_L - (1-u) v_o \\ C_f \frac{dv_o}{dt} = & (1-u) i_L - i_o \end{cases} \tag{14}$$

where $u \in \{0,1\}$ i.e., $u = 0$ when $\mathbf{S}_{12} = (S_1, S_2) = (0,1)$, and $u = 1$ when $\mathbf{S}_{12} = (1,0)$. By Euler's forward discretization, the state predictions are

$$\begin{cases} i_L(k+1) = \left(1 - \frac{R_f T_s}{L_f}\right) \bar{i}_L(k) + \frac{T_s}{L_f} \left(v_{in}(k) - (1-u) v_o(k)\right) \\ v_o(k+1) = v_o(k) + \frac{T_s}{C_f} \left((1-u) \bar{i}_L(k) - i_o(k)\right) \end{cases} \tag{15}$$

where $\bar{i}_L = 0.5(i_L(k) + i_L(k+1))$ is the average inductor current between two samples.

1) Current Reference: The power balance between input and output leads to the reference current [28]

$$i_L^*(k+) = \frac{2 v_o(k) i_o(k)}{v_{in}(k)} - i_L(k) + k_{pL} T_s (v_o^*(k) - v_o(k)) \tag{16}$$

where k_{pL} is the proportional controller gain.

2) Optimization: To achieve current control, the optimization problem entails minimizing the cost function

$$J_b(k) = (i_L(k+1) - i_L^*(k+1))^2 \tag{17}$$

subject to constraints of the maximum inductor current $i_L^{\max}$, and maximum output voltage $v_o^{\max}$ (e.g., whenever $i_L^*(k+1) \geq i_L^{\max}$, $i_L^{\max}$ is used as the reference).

B. Model-Free Predictive Control

The ultralocal model of the inductor current dynamics is

$$\frac{di_L}{dt} = F + \alpha u \tag{18}$$

where F is the total disturbance term that subsumes $\frac{1}{L_f}(v_{\text{in}} - R i_L - v_o)$; and α is the control input gain with an initial tuning value of $\alpha_0 = \frac{v_o}{L}$ [24]. The standard ESO predicts estimates for i_L and F, respectively, as

$$\begin{cases} \hat{i}_L(k+1) = \hat{i}_L(k) + T_s(\hat{F}(k) + \alpha u(k)) - \gamma_1(\hat{i}_L(k) - i_L^m(k)) \\ \hat{F}(k+1) = \hat{F}(k) - \gamma_2(\hat{i}_L(k) - i_L^m(k)) \end{cases} \tag{19}$$

where $\{\gamma_1, \gamma_2\} = \{2T_s\omega_0,\ T_s\omega_0^2\}$ are the observer gains, T_s is the sampling time, and i_L^m is the measured inductor current. Reference current and cost function are computed from (16), (17), respectively, by substituting i_L with $\hat{i}_L$. The predicted output voltage is

$$v_o(k+1) = v_o(k) + \frac{T_s}{C_f} \left((1-u)\hat{i}_L(k) - i_o(k)\right). \tag{20}$$

C. Proposed Model-Free Control With Noise Suppression

In order to attenuate measurement noise, PC-ESO and CP-ESO (modeled in Section III-B) will be employed for state predictions.

1) PC-ESO Discretization: PC-ESO-3 modeled in Table II has discretized subfrequency estimates as

$$\begin{cases} \hat{i}_{L1}(k+1) = \hat{i}_{L1}(k) + T_s(\hat{F}_1(k) + \alpha u(k)) - T_s \gamma_{11}(\hat{i}_{L.m}(k)) \\ \hat{F}_1(k+1) = \hat{F}_1(k) - T_s \gamma_{21}(\hat{i}_{L.m}(k)) \\ \hat{i}_{L2}(k+1) = \hat{i}_{L2}(k) + T_s(\hat{F}_2(k) + \alpha u(k)) - T_s \gamma_{12}(\hat{i}_{L.m}(k)) \\ \hat{F}_2(k+1) = \hat{F}_2(k) - T_s \gamma_{22}(\hat{i}_{L.m}(k)) \\ \hat{i}_{L3}(k+1) = \hat{i}_{L3}(k) + T_s(\hat{F}_3(k) + \alpha u(k)) - T_s \gamma_{13}(\hat{i}_{L2.1}(k)) \\ \hat{F}_3(k+1) = \hat{F}_3(k) - T_s \gamma_{23}(\hat{i}_{L2.1}(k)) \end{cases} \tag{21}$$

where T_s is the sampling time, $\hat{i}_{L.m}(k) = \hat{i}_L(k) - i_L^m(k)$, $\hat{i}_{L2.1}(k) = \hat{i}_{L2}(k) - i_{L1}(k)$, and all other variables are as earlier defined in Section III.

$\hat{F}_j(k+1)$ terms in (21) are inputs for the predicted inductor current and total disturbance estimated by PC-ESO

$$\begin{cases}\hat{i}_L(k+1)=\hat{i}_L(k)+T_s\left(\sum_{j=1}^{3}\hat{F}_j(k+1)+\alpha u(k)\right)-\hat{i}_\gamma \\ \hat{F}(k+1)=\hat{F}(k)-\hat{F}_\gamma\end{cases} \tag{22}$$

where $\hat{i}_\gamma=\frac{1}{2}(\gamma_{11}+\gamma_{31})(\hat{i}_L(k)+\hat{i}_{L3}(k)-i_L^m(k)-\hat{i}_{L2}(k))$, and $\hat{F}_\gamma=\frac{1}{2}(\gamma_{12}+\gamma_{32})(\hat{i}_L(k)+\hat{i}_{L3}(k)-i_L^m(k)-\hat{i}_{L2}(k))$. Output voltage prediction is computed with (20).

Remark: The direct expressions for $\hat{i}_\gamma$ and $\hat{F}_\gamma$ from the PC-ESO structure in Fig. 3 are $\hat{i}_\gamma=\frac{1}{2}\gamma_{11}(\hat{i}_L(k)-i_L^m(k))+\frac{1}{2}\gamma_{31}(\hat{i}_{L3}(k)-\hat{i}_{L2}(k))$, and $\hat{F}_\gamma=\frac{1}{2}\gamma_{12}(\hat{i}_L(k)-i_L^m(k))+\frac{1}{2}\gamma_{32}(\hat{i}_{L3}(k)-\hat{i}_{L2}(k))$. Since the gains are halved, this will cause slower response and poorer disturbance rejection. This informs the formulation in (22) with the average of gains.

2) CP-ESO Discretization: CP-ESO-3 A modeled in Table II has discretized subfrequency estimates as

$$\begin{cases}\hat{i}_{L1}(k+1)=\hat{i}_{L1}(k)+T_s(\hat{F}_1(k)+\alpha u(k))-T_s\gamma_{11}(\hat{i}_{L.m}(k)) \\ \hat{F}_1(k+1)=\hat{F}_1(k)-T_s\gamma_{21}(\hat{i}_{L.m}(k)) \\ \hat{i}_{L2}(k+1)=\hat{i}_{L2}(k)+T_s(\hat{F}_2(k)+\alpha u(k))-T_s\gamma_{12}(\hat{i}_{L2.1}(k)) \\ \hat{F}_2(k+1)=\hat{F}_2(k)-T_s\gamma_{22}(\hat{i}_{L2.1}(k)) \\ \hat{i}_{L3}(k+1)=\hat{i}_{L3}(k)+T_s(\hat{F}_3(k)+\alpha u(k))-T_s\gamma_{13}(\hat{i}_{L3.1}(k)) \\ \hat{F}_3(k+1)=\hat{F}_3(k)-T_s\gamma_{23}(\hat{i}_{L3.1}(k))\end{cases} \tag{23}$$

where T_s is the sampling time, $\hat{i}_{L.m}(k)=\hat{i}_L(k)-i_L^m(k)$, $\hat{i}_{L2.1}(k)=\hat{i}_{L2}(k)-i_{L1}(k)$, $\hat{i}_{L3.1}(k)=\hat{i}_{L3}(k)-i_{L1}(k)$, and all other variables are as earlier defined in Section III.

$\hat{F}_j(k+1)$ terms in (23) are inputs for the predicted inductor current and total disturbance estimated by CP-ESO

$$\begin{cases}\hat{i}_L(k+1)=\hat{i}_L(k)+T_s\left(\sum_{j=1}^{3}\hat{F}_j(k+1)+\alpha u(k)\right)-\hat{i}_\gamma \\ \hat{F}(k+1)=\hat{F}(k)-\hat{F}_\gamma\end{cases} \tag{24}$$

where $\hat{i}_\gamma=\frac{1}{2}T_s(\gamma_{12}+\gamma_{13})(\hat{i}_{L2}(k)+\hat{i}_{L3}(k)-2\hat{i}_{L1}(k))$, and $\hat{F}_\gamma=\frac{1}{2}T_s(\gamma_{22}+\gamma_{23})(\hat{i}_{L2}(k)+\hat{i}_{L3}(k)-2\hat{i}_{L1}(k))$. Output voltage prediction is computed with (20).

3) Adaptive Operation: Performance improvements can be obtained from both PC-ESO and CP-ESO when their parameters are adapted to dynamic system conditions. Transient state is active if the total change in absolute value of i_o over four consecutive samples exceeds a preset threshold.

a) PC-ESO Adaptive Mode: A closer inspection of $\hat{i}_\gamma$ and $\hat{F}_\gamma$ in (22) reveals that they have common current sums that comprise a *disturbance rejection* and a *noise suppression* term. Hence, adapting the relative weights of these terms can modify the characteristics of PC-ESO's results. During adaptive mode, the *disturbance rejection* term is weighted by $\chi_{pc}\in\{0,1\}$, and the *noise suppression* term is weighted by $(1-\chi_{pc})$ as follows:

$$\begin{cases}\hat{i}_{\gamma\_\text{adapt}}=\chi_{pc}(\gamma_{11}+\gamma_{31})(\hat{i}_L(k)-i_L^m(k)) \\ +(1-\chi_{pc})(\gamma_{11}+\gamma_{31})(\hat{i}_{L3}(k)-\hat{i}_{L2}(k)) \\ \hat{F}_{\gamma\_\text{adapt}}=\chi_{pc}(\gamma_{12}+\gamma_{32})(\hat{i}_L(k)-i_L^m(k)) \\ +(1-\chi_{pc})(\gamma_{12}+\gamma_{32})(\hat{i}_{L3}(k)-\hat{i}_{L2}(k)).\end{cases} \tag{25}$$

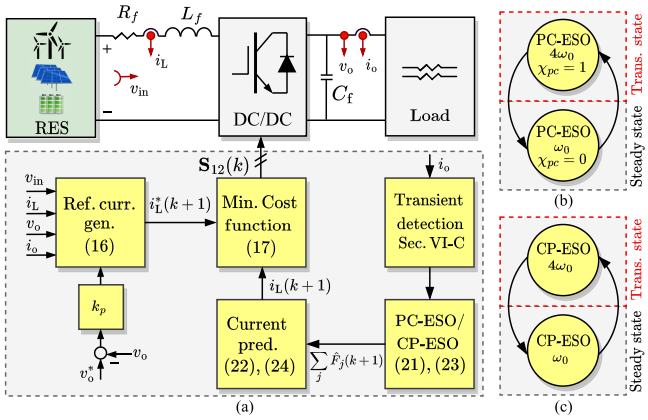

Fig. 9. Proposed MFPC of a bidirectional DC–DC boost converter. (a) Overall control. (b) Adaptive PC-ESO. (c) Adaptive CP-ESO.

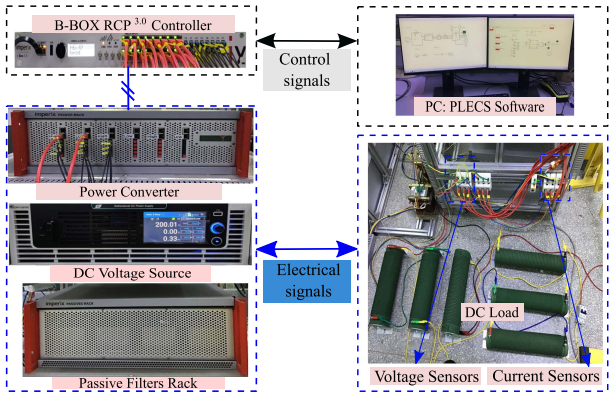

Fig. 10. Experimental test bench.

PC-ESO's adaptive mode is useful when there is high measurement noise: during steady state, $\chi_{pc}=0$, and during transient state $\chi_{pc}=1$ [see Fig. 9(b)].

b) CP-ESO Adaptive Mode: The intrinsic disturbance rejection for CP-ESO is weaker than ESO-1. Therefore, adaptive methods are necessary. This article proposes a *full adaptive* structure: both current and total disturbance are computed with a higher bandwidth ($4\omega_0$ in this article) during transients, and by the normal bandwidth during steady-state [see Fig. 9(c)]. This is different from [24] that applied a *split adaptive* structure.

VII. Experimental Validation and Discussion

The overall proposed control scheme is illustrated in Fig. 9. It was experimentally validated on a laboratory test bench [see Fig. 10]. PLECS software was used to generate the codes for Imperix B-BOX RCP $^{3.0}$ to control the power converter comprising two silicon carbide MOSFETs and passive filters. The ADCs are 16-bit ADS8568 from Texas Instruments. The rapid control prototyping setup includes dual-core ARM processor and FPGA. The system was tested under two cases: output voltage $v_o=40$ V (*Case A*), and $v_o=150$ V (*Case B*). The key parameters of the system are: filter parameters $L_f=2.3$ mH, $C_f=1e3$ μ F, load resistance $R_L=40\ \Omega$, sampling frequency $f_s=20$ kHz, proportional controller gain $k_{pb}=15$,

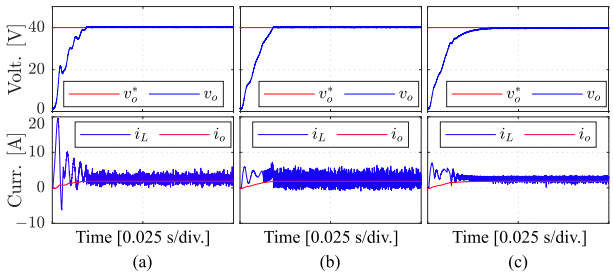

Fig. 11. [Experimental results:] Startup current control. (a) CESO. (b) PC-ESO. (c) CP-ESO.

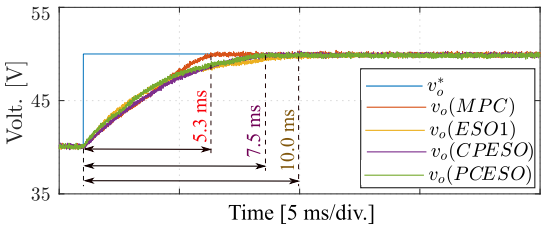

Fig. 12. [Experimental results:] Output v_o reference tracking.

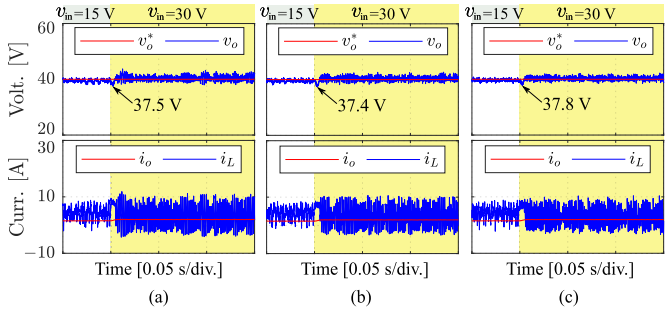

Fig. 13. [Experimental results:] Step change of input voltage (*Case A*). (a) CESO. (b) Proposed CP-ESO. (c) Proposed PC-ESO.

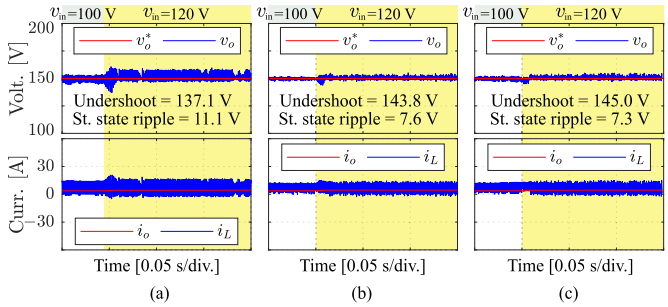

Fig. 14. [Experimental results:] Step change of input voltage (*Case B*, $\omega_0 = 1e3$). (a) CESO. (b) Proposed CP-ESO. (c) Proposed PC-ESO.

bandwidth $\omega_0 = 3e3$ rad/s. *Case A:* $v_{\text{in}} = 30$ V, control input gains α for ESO-1, CESO, PC-ESO and CP-ESO, respectively, are $\{2.5e4,\ 2.65e4, 3.1e4, 1.75e4\}$, and inductor current limit $i_L^{\max} = 10$ A. *Case B:* $v_{\text{in}} = 80$ V, control input gains α for ESO-1, CESO, PC-ESO, and CP-ESO, respectively, are $\{6e4,\ 54, 5e4, 6e4\}$, and $i_L^{\max} = 15$ A. $v_o^{\max} = v_o^*$ for both cases. Hybrid ESO parameters are designed, as described in Section II-I-C.

a) Startup Performance: The poorer disturbance estimations of CESO (and other hybrid ESO with cascade structures) cause higher startup current when tuned for good noise suppression. Therefore, the adaptive schemes discussed in Section VI-C3 limit inrush currents for PC-ESO and CP-ESO. Fig. 11 shows that the startup current is effectively reduced from 19.8 A (CESO) to 7.2 A (for PC-ESO and CP-ESO) to protect the power converter from overcurrents.

b) Step Change in Output Reference Voltage: The response to step change in output reference voltage from 40 to 50 V is shown in Fig. 12. The proposed PC-ESO and CP-ESO were capable of accurately tracking the designated references. The rise times of both PC-ESO and CP-ESO (at $M = 1.05$, when they are not tuned for noise suppression) are faster than that of the standard ESO (ESO-1) by 2.5 ms.

MPC is not affected by the ESO bandwidth; hence, it has the fastest dynamic response. The experimental tests were done at a relatively low ESO bandwidth $\omega_0 = 3e3$ rad/s (typical in related literature e.g., [22], [23]), hence the dynamic responses of all the ESOs are slower than MPC's. However, when ω_0 is increased to $20e3$ rad/s, all the ESOs have identically fast dynamic response as MPC's (not shown).

c) Step Change in Input Voltage: Since renewable energy sources experience weather-induced output variability, it is necessary for the control performance to be robust to variable input voltage v_{in}. The impact of a step change of input voltage v_{in} from 15 to 30 V for *Case A* is shown in Fig. 13. The proposed ESOs effectively regulated the output voltage to the reference. In Fig. 13, the proposed PC-ESO produced lower undershoot and ripples than the conventional CESO. Furthermore, for *Case B* in Fig. 14, reducing ω_0 to $1e3$ rad/s shows the superior disturbance rejection of the proposed methods over CESO under low ESO bandwidth (ESO-1, not shown, has identical performance to CP-ESO).

d) Step Change in Load: In Fig. 15, for *Case A*, the load was decreased by 50%, resulting in a rise in inductor and load currents. CESO was unable to regulate v_o to the reference after the disturbance. However, the two proposed methods effectively rejected the disturbance and sustained accurate reference tracking, due to the adaptive schemes. In Fig. 16 (*Case B*), when the load was decreased by 25%, the proposed methods sustained the v_o^* tracking.

e) Noise Suppression Performance: The measured inductor current was summed with white noise of standard deviation 3.0. The comparative performances of six control methods are shown in Fig. 17 for *Case A*. The measurement noise increased the inductor current i_L ripples significantly for both MPC and ESO-1. However, the proposed PC-ESO and CP-ESO were effective in suppressing the impact of noise, resulting in much lower i_L ripples: 3.97 A for CP-ESO, and 4.28 A for PC-ESO versus 9.0 A for MPC. In addition, the proposed methods produced the lowest output voltage ripples among the compared methods: 25.0% and 18.8% less ripples for CP-ESO and PC-ESO, respectively, than MPC. ESO-1 at

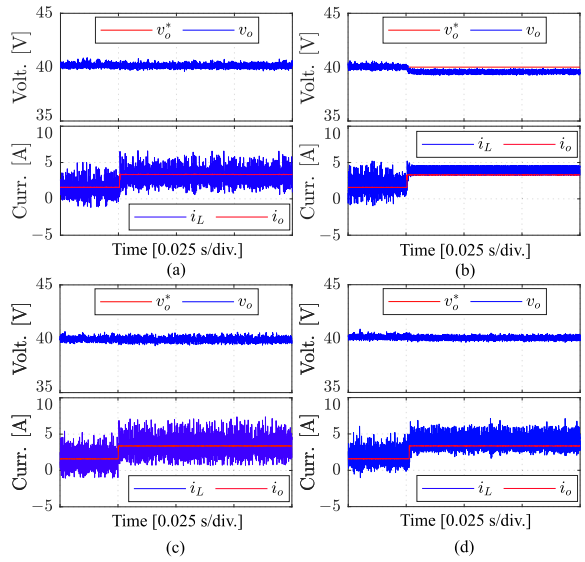

Fig. 15. [Experimental results:] Step change of resistive load *(Case A)*. (a) ESO1. (b) CESO. (c) PC-ESO. (d) CP-ESO.

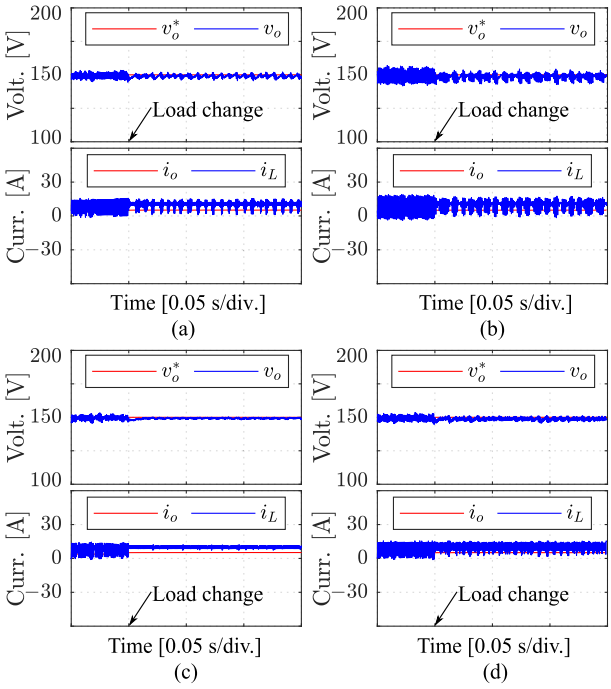

Fig. 16. [Experimental results:] Step change of resistive load *(Case B)*. (a) ESO-1. (b) CESO. (c) Proposed CP-ESO. (d) Proposed PC-ESO.

lower bandwidth of 500 rad/s [see Fig. 17(c)] produced identical i_L noise suppression as CP-ESO, but at 35% longer rise time.

Noise suppression performances for *Case B* are shown in Fig. 18. The proposed methods have 57.3% (for CP-ESO) and 54.9% (for PC-ESO) lower steady-state ripples than MPC. The proposed PC-ESO has 13.3% faster rise time and 5.5% lower steady state ripples than ESO-1. The ESO-based methods are

TABLE IV
SUMMARY OF EXPERIMENTAL RESULTS

	MPC	ESO-1	CESO	PC-ESO	CP-ESO
Noise i_L ripple (A)	8.960	7.980	6.780	4.280	3.970
Noise v_o ripple (V)	0.800	0.800	0.650	0.650	0.600
Mismatch $\lvert\Delta v_o\rvert$ (%)	18.750	4.500	7.250	1.500	6.250
Comp. time (μs)	2.734	2.669	3.142	3.069	3.141

Yellow highlights: key indices improved by this study.

slower than MPC for reasons earlier explained in Section VII-*b*. Furthermore, for a balance between noise suppression and speed of dynamic response, CP-ESO's noise tuning parameter was set to $M = 1.5$. Higher values of M for CP-ESO give better noise suppression with slower dynamic response.

f) Mode Change Performance: Fig. 19 shows the performance of the proposed method under sudden change from charging mode to discharging mode. The results demonstrate the ability of the proposed methods to support effective and stable mode-change performance. The charging voltage (40 V) and current (2.4 A) are the nominal values for Fig. 19.

g) Robustness to Parameter Mismatches: The controlled system was subjected to parameter mismatches of $\{0.5L_f, 1.5L_f\}$ for all the compared methods in *Case A*. The proposed PC-ESO and CP-ESO had v_o variations of 1.5% and 6.25%, respectively, while MPC had 18.75% variation (see Fig. 20 and Table IV). Δv_o is the maximum percentage change in ripples (due to mismatch) relative to nominal parameter conditions. Dynamic performance was also tested under parameter mismatches of $\{0.2L_f, 5L_f\}$ (values that distinguish the robustness differences of the compared methods) for *Case B*, when v_{in} was changed from 100 to 120 V. The results shown in Figs. 21 and 22 show that while MPC is severely influenced by model parameter mismatches, the proposed methods are robust to parameter uncertainties. All the control methods had negligible sensitivity to parameter mismatch of C_f, so the results are not shown.

h) High Sampling Frequency Performance: The performances of the proposed methods were validated at a high sampling rate of 1.0 MHz, which is typical of high-density power electronic applications. For all the dynamic changes of input voltage (see Fig. 23) and load change (see Fig. 24), the dynamic response and disturbance rejection of the proposed methods were not deteriorated—including under measurement noise conditions (see Fig. 25). At high sampling frequencies (above 150 kHz), high-frequency-induced noises in power converters are more dominant than at lower frequencies [9]. The results in Fig. 25 show that the proposed methods are insufficient *alone* to suppress the combined noises generated at high sampling frequencies. Thus, complementary techniques for high-frequency noise mitigation will be beneficial e.g., spread-spectrum modulation, gate driver optimization, and appropriate passive/active filter design [29].

i) Computational Time: The average computation time, per sampling period, during steady state, is shown in Table IV.

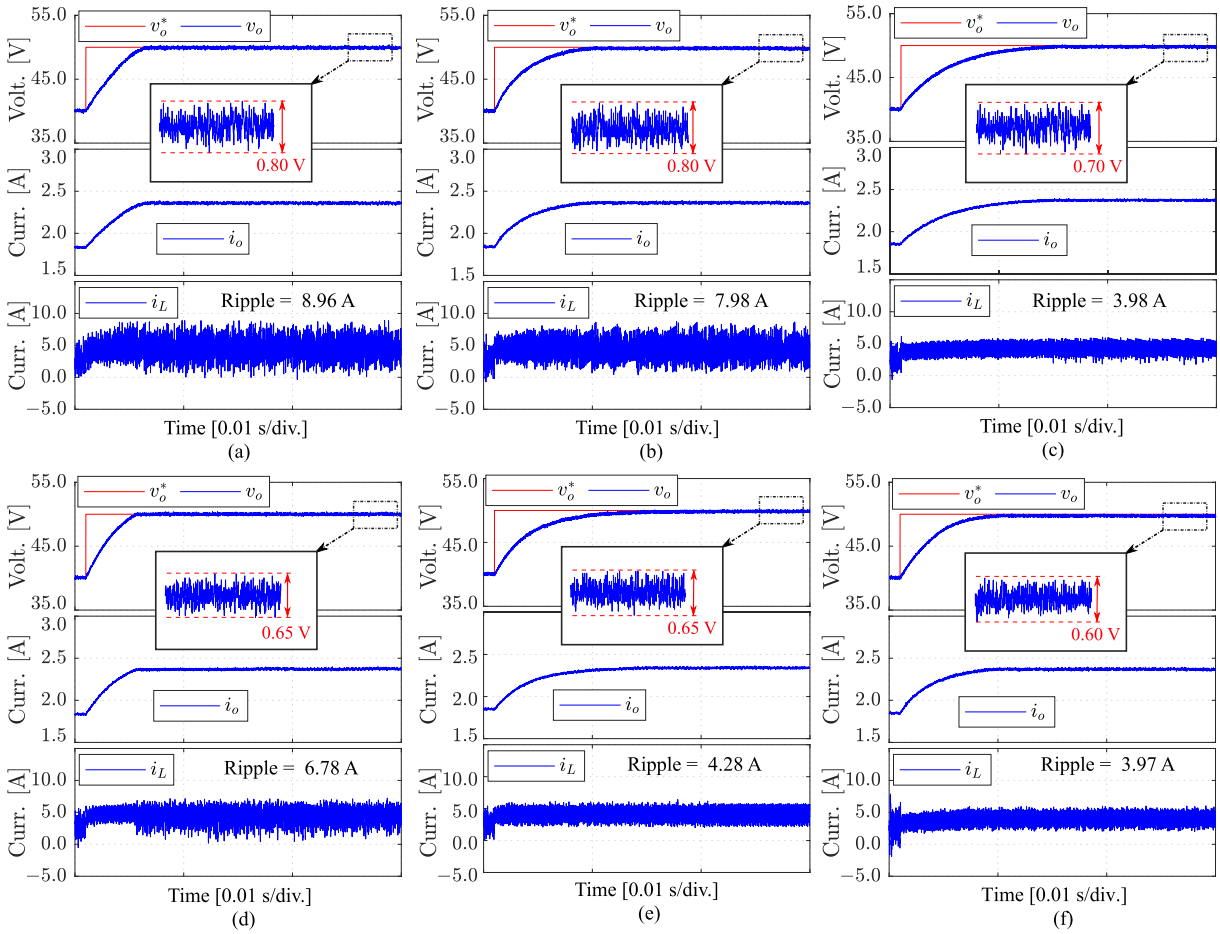

Fig. 17. [Experimental results:] Noise suppression performance (*Case A*). (a) MPC. (b) ESO-1. (c) ESO-1 at lower bandwidth. (d) CESO. (e) Proposed PC-ESO. (f) CP-ESO.

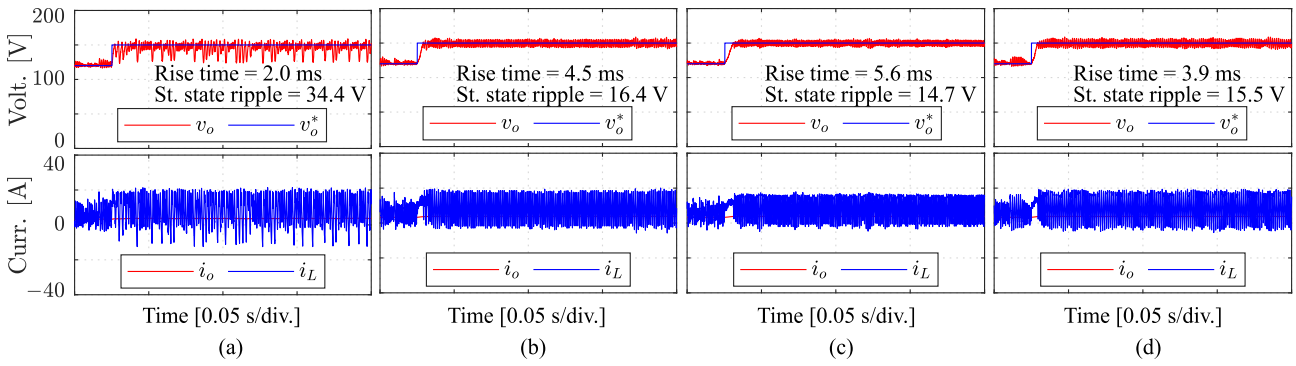

Fig. 18. [Experimental results:] Noise suppression performance (*Case B*). (a) MPC. (b) ESO-1. (c) Proposed CP-ESO. (d) Proposed PC-ESO.

The proposed PC-ESO- and CP-ESO-based predictive control lower ripples and better robustness than CESO, while requiring 2.32% lower computation time, and about the same time than CESO, respectively. The proposed methods can improve the noise suppression performance by up to 55.6% with a slight increase of 15.88% in the computation time than conventional MPC or ESO-1.

j) Overall Experimental Performance: PC-ESO and CP-ESO produced the best noise suppression and robustness results. Measurement noise-induced ripples (for *Case A*) were reduced by up to 55.6% and 25%, respectively, for i_L and v_o. Although CP-ESO's noise suppression is superior to the PC-ESO's, the proposed PC-ESO has better robustness to parameter variations than CP-ESO. These superior results for PC-ESO and CP-ESO,

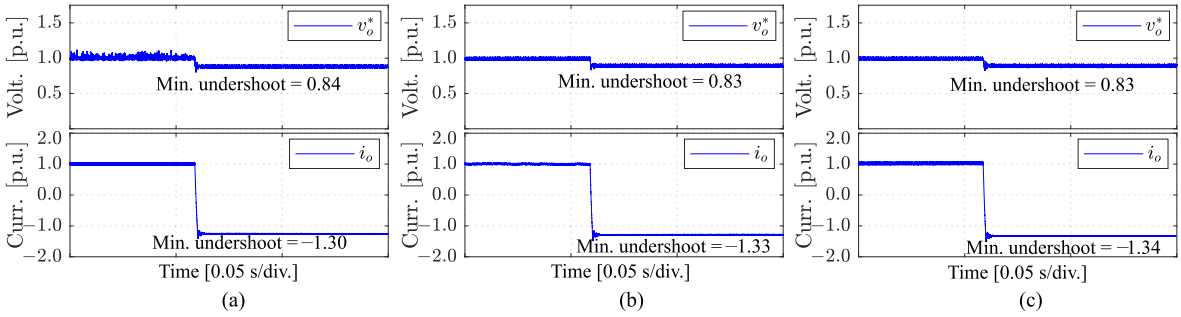

Fig. 19. [Experimental results:] Mode change performance. (a) MPC. (b) CP-ESO. (c) Proposed PC-ESO.

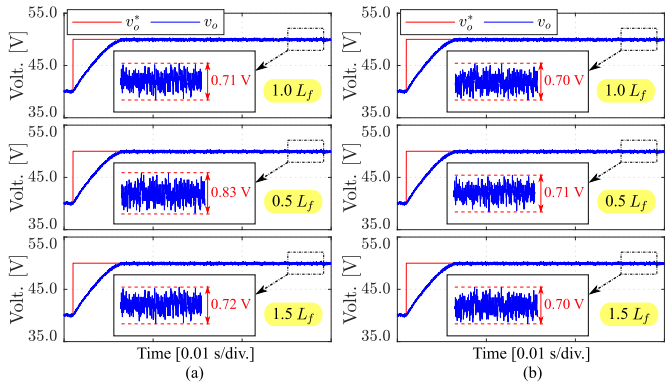

Fig. 20. [Experimental results:] Parameter mismatch (*Case A*). (a) MPC. (b) Proposed PC-ESO.

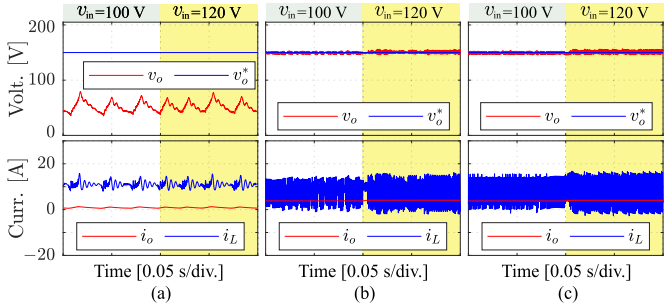

Fig. 21. [Experiments:] $0.2L_f$ parameter mismatch (*Case B*). (a) MPC. (b) Proposed CP-ESO. (c) Proposed PC-ESO.

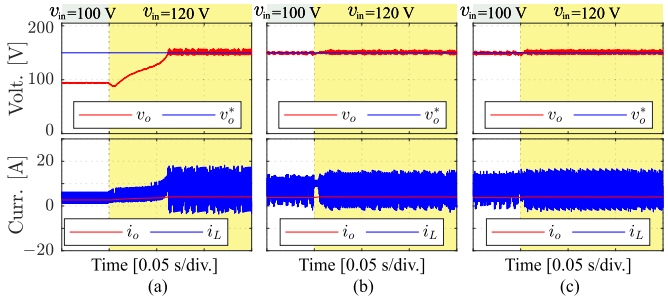

Fig. 22. [Experiments:] $5L_f$ parameter mismatch (*Case B*). (a) MPC. (b) Proposed CP-ESO. (c) Proposed PC-ESO.

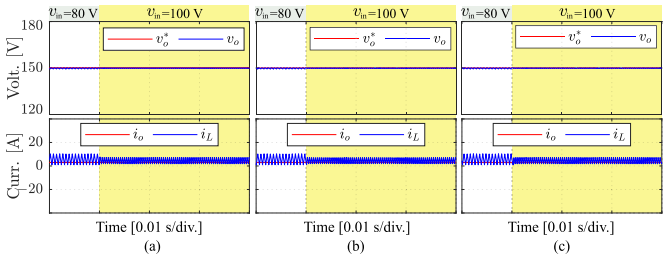

Fig. 23. Simulation of step change of input voltage at high switching frequency (*Case B*). (a) MPC. (b) Proposed CP-ESO. (c) Proposed PC-ESO.

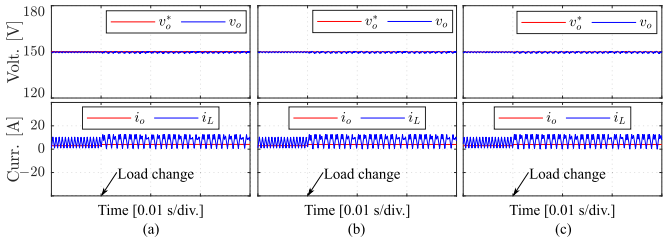

Fig. 24. Simulation of load change at high switching frequency (*Case B*). (a) MPC. (b) Proposed CP-ESO. (c) Proposed PC-ESO.

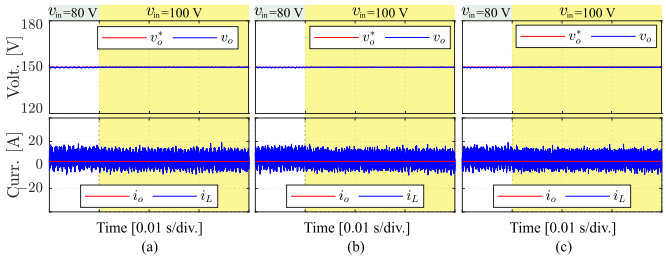

Fig. 25. Simulation of dynamic performance with measurement noise at high switching frequency (*Case B*). (a) MPC. (b) Proposed CP-ESO. (c) Proposed PC-ESO.

from Figs. 17 and 20 (summarized in Table IV for *Case A*) were achieved without an increase of the computation time over CESO's.

VIII. Conclusion

The model predictive control of bidirectional boost converters applied to renewable energy sources deteriorates due to sensor measurement noises and model uncertainties. Therefore, this study proposed a new ESO to mitigate the dual challenges: the hybrid PC-ESO. PC-ESO is an ultralocal MF-ESOs with intrinsically better noise suppression, than the ESO-1. Several higher order structures for both PC-ESO and the CP-ESO were also introduced. Comprehensive theoretical analyses show that the proposed hybrid ESOs produce superior frequency-domain disturbance estimation and noise suppression that *neither the conventional ESO or cascade ESO can produce alone.* Experimental results validate the effectiveness of the proposed hybrid ESOs in for robust predictive control of the BDBC. Measurement noise-induced ripples were reduced by 55.6% and 25%, respectively, for inductor current and output voltage. In future studies, we shall apply the proposed methods to multiphase interleaved dc–dc converters and other dc–dc converter topologies as well.

References

[1] S. A. Gorji, H. G. Sahebi, M. Ektesabi, and A. B. Rad, "Topologies and control schemes of bidirectional DC–DC power converters: An overview," *IEEE Access*, vol. 7, pp. 117997–118019, 2019.

[2] Y. Li, Z. Zhang, and R. Kennel, "A full state-variable predictive control of bi-directional boost converters with guaranteed stability," in *Proc. 22nd Eur. Conf. Power Electron. Appl.*, 2020, pp. P.1–P.7.

[3] M. M. Mardani, M. H. Khooban, A. Masoudian, and T. Dragicevic, "Model predictive control of DC-DC converters to mitigate the effects of pulsed power loads in naval DC microgrids," *IEEE Trans. Ind. Electron.*, vol. 66, no. 7, pp. 5676–5685, Jul. 2019.

[4] Y. Shan, J. Hu, K. W. Chan, Q. Fu, and J. M. Guerrero, "Model predictive control of bidirectional DC-DC converters and AC/DC interlinking converters—a new control method for PV-wind-battery microgrids," *IEEE Trans. Sustain. Energy*, vol. 10, no. 4, pp. 1823–1833, Oct. 2019.

[5] J. Rodriguez et al., "Latest advances of model predictive control in electrical drives—part ii: Applications and benchmarking with classical control methods,," *IEEE Trans. Power Electron.*, vol. 37, no. 5, pp. 5047–5061, May 2022.

[6] J. Luna, E. Usai, A. Husar, and M. Serra, "Enhancing the efficiency and lifetime of a proton exchange membrane fuel cell using nonlinear model-predictive control with nonlinear observation," *IEEE Trans. Ind. Electron.*, vol. 64, no. 8, pp. 6649–6659, Aug. 2017.

[7] J. Yang, J. Liu, J. Zhang, N. Zhao, Y. Wang, and T. Q. Zheng, "Multirate digital signal processing and noise suppression for dual active bridge DC–DC converters in a power electronic traction transformer," *IEEE Trans. Power Electron.*, vol. 33, no. 12, pp. 10885–10902, Dec. 2018.

[8] I. Z. Petric, P. Mattavelli, and S. Buso, "Feedback noise propagation in multisampled DC–DC power electronic converters," *IEEE Trans. Power Electron.*, vol. 37, no. 1, pp. 150–161, Jan. 2022.

[9] S. Inoue, M. Ishigaki, A. Takahashi, and T. Sugiyama, "Design of an isolated bidirectional DC–DC converter with built-in filters for high power density," *IEEE Trans. Power Electron.*, vol. 36, no. 1, pp. 739–750, Jan. 2021.

[10] K. Bi et al., "A model predictive controlled bidirectional four quadrant flying capacitor DC/DC converter applied in energy storage system," *IEEE Trans. Power Electron.*, vol. 37, no. 7, pp. 7705–7717, Jul. 2022.

[11] V. Jayan and A. M. Y. M. Ghias, "A single-objective modulated model predictive control for a multilevel flying-capacitor converter in a DC microgrid," *IEEE Trans. Power Electron.*, vol. 37, no. 2, pp. 1560–1569, Feb. 2022.

[12] L. Po, L. Ruiyu, S. Tianying, Z. Jingrui, and F. Zheng, "Composite adaptive model predictive control for DC–DC boost converters," *IET Power Electron.*, vol. 11, no. 10, pp. 1706–1717, Oct. 2018.

[13] L. Cheng et al., "Model predictive control for DC–DC boost converters with reduced-prediction horizon and constant switching frequency," *IEEE Trans. Power Electron.*, vol. 33, no. 10, pp. 9064–9075, Oct. 2018.

[14] P. Karamanakos, T. Geyer, and S. Manias, "Direct voltage control of DC–DC boost converters using enumeration-based model predictive control," *IEEE Trans. Power Electron.*, vol. 29, no. 2, pp. 968–978, Feb. 2014.

[15] Z. Karami, Q. Shafiee, S. Sahoo, M. Yaribeygi, H. Bevrani, and T. Dragicevic, "Hybrid model predictive control of DC–DC boost converters with constant power load," *IEEE Trans. Energy Convers.*, vol. 36, no. 2, pp. 1347–1356, Jun. 2021.

[16] F. Bento, I. Jlassi, and A. J. M. Cardoso, "Model-free predictive control of interleaved DC-DC converters, based on ultra-local model, with constant switching frequency," in *Proc. IEEE Energy Convers. Congr. Expo.*, 2021, pp. 2022–2028.

[17] J. Sawma, F. Khatounian, E. Monmasson, L. Idkhajine, and R. Ghosn, "Robustness study of a cascaded dual model-predictive control applied to synchronous motors," *IEEE Trans. Ind. Electron.*, vol. 66, no. 9, pp. 7219–7228, Sep. 2019.

[18] S. Wang, T. Dragicevic, G. F. Gontijo, S. K. Chaudhary, and R. Teodorescu, "Machine learning emulation of model predictive control for modular multilevel converters," *IEEE Trans. Ind. Electron.*, vol. 68, no. 11, pp. 11628–11634, Nov. 2021.

[19] D. Pérez-Estévez and J. Doval-Gandoy, "A model predictive current controller with improved robustness against measurement noise and plant model variations," *IEEE Open J. Ind. Appl.*, vol. 2, pp. 131–142, Apr. 2021.

[20] H. Sartipizadeh, F. Harirchi, M. Babakmehr, and P. Dehghanian, "Robust model predictive control of DC-DC floating interleaved boost converter with multiple uncertainties," *IEEE Trans. Energy Convers.*, vol. 36, no. 2, pp. 1403–1412, Jun. 2021.

[21] K. Łakomy and R. Madonski, "Cascade extended state observer for active disturbance rejection control applications under measurement noise," *ISA Trans.*, vol. 109, pp. 1–10, Mar. 2021.

[22] K. Łakomy et al., "Active disturbance rejection control design with suppression of sensor noise effects in application to DC–DC buck power converter," *IEEE Trans. Ind. Electron.*, vol. 69, no. 1, pp. 816–824, Jan. 2022.

[23] S. Ahmad and A. Ali, "On active disturbance rejection control in presence of measurement noise," *IEEE Trans. Ind. Electron.*, vol. 69, no. 11, pp. 11600–11610, Nov. 2022.

[24] O. Babayomi and Z. Zhang, "Model-free predictive control of power converters with cascade-parallel extended state observers," *IEEE Trans. Ind. Electron.*, vol. 70, no. 10, pp. 10215–10226, Oct. 2023.

[25] M. Fliess and C. Join, "Model-free control," *Int. J. Control*, vol. 86, no. 12, pp. 2228–2252, Dec. 2013.

[26] O. Babayomi and Z. Zhang, "Model-free predictive control of power converters with multi-frequency extended state observers," *IEEE Trans. Ind. Electron.*, vol. 70, no. 11, pp. 11379–11389, Nov.. 2023.

[27] Z. Gao, "Scaling and bandwidth-parameterization based controller tuning," in *Proc. Amer. Control Conf.*, 2003, vol. 6, pp. 4989–4996.

[28] Y. Li, Z. Zhang, T. Dragicevic, and J. Rodriguez, "A unified distributed cooperative control of DC microgrids using consensus protocol," *IEEE Trans. Smart Grid*, vol. 12, no. 3, pp. 1880–1892, May 2021.

[29] S. Xu, S. Xu, D. Xu, Q. Qian, W. Sun, and J. Zhu, "A review on recent effort of conductive EMI suppression methods in high-frequency power converters," *IET Power Electron.*, vol. 15, no. 16, pp. 1921–1935, 2022.

Oluleke Babayomi (Senior Member, IEEE) received the B.Sc. (Hons) and M.Sc. degrees in electrical and electronics engineering from the University of Lagos, Lagos, Nigeria, in 2006 and 2016, respectively, and the Ph.D. degree in electrical engineering from Shandong University, Jinan, China in 2023.

He is currently a Postdoctoral Researcher with the Korea Advanced Institute of Science and Technology, Daejeon, South Korea. Until 2019, he was a Principal Engineer and software development Team Lead with National Space Research and Development Agency, Nigeria. His research interests include model predictive control, power electronics, microgrids, and sustainable energy policy.

Dr. Babayomi is the 2023–2024 Chair of the IEEE Smart Village Marketing Committee.

Zhenbin Zhang (Senior Member, IEEE) received the Ph.D. (*summa cum laude*) degree in electrical and energy engineering from the Technical University of Munich, Munich, Germany, in 2016.

Since 2017, he has been a Full Professor with Shandong University, Jinan, China, where he is currently the Director for both the Laboratory of More Power Electronics Energy Systems and the Institute of Sustainable Energy and Smart Grids. He was a Postdoctoral Researcher of electrical and energy engineering with the Technical University of Munich. His research interests include power electronics and electrical drives, sustainable energy systems, smart grids, and microgrids.

Dr. Zhang was the recipient of the VDE Award 2017, Germany. He is an Associate Editor for IEEE TRANSACTIONS POWER ELECTRONICS. He is a Fellow and Chartered Engineer of the Institution of Engineering and Technology.

Zhen Li (Member, IEEE) received the Ph.D. degree in power electronic semiconductor materials from Friedrich Alexander University Erlangen Nörnberg (FAU), Erlangen, Germany, in 2017.

Since 2019, she has been an Associate Professor with Shandong University, Jinan, China. From 2014 to 2015, she was a Teaching and Research Assistant with FAU. Her research interests include reliable design and control of power converters, and energy conversion systems.